Pore-scale study of the multiphase methane hydrate dissociation dynamics and mechanisms in the sediment

Junyu Yang [a], Qianghui Xu [a]*, Zhiying Liu [a] and Lin Shi [a]

[a] Key Laboratory for Thermal Science and Power Engineering of Ministry of Education, Department of Energy and Power Engineering, Tsinghua University, Beijing 100084, China.

* xuqh12@tsinghua.org.cn

Highlights

1. Multiphase pore-scale modelling of the hydrate dissociation is investigated

2. Effects of the water saturation and Péclet number on the hydrate dissociation are revealed

3. The mass-transfer-limitation and heat-transfer-limitation on hydrate dissociation are quantified

4. Regime diagram of the hydrate dissociation are mapped

5. Empirical models of the permeability and specific surface area are obtained

Abstract

Methane hydrate is a promising energy resource, but the hydrate development still faces technical difficulties due to the complicated multiple physicochemical and thermal processes during the multiphase hydrate dissociation in the sediment. In this study, a pore-scale numerical model based on the lattice Boltzmann method was proposed to simulate methane hydrate dissociation considering multiphase flow, heat and species transport, heterogeneous reaction and hydrate structure evolution. The single-phase hydrate dissociation was firstly simulated to identify the convection and diffusion transport-limited regimes according to the Péclet number. Effects of the connate water saturation and the Péclet number on the multiphase hydrate dissociation were then investigated to understand the varying dissociation dynamics and dissociation mechanisms. The competitive mass-transfer-limitation and heat-transfer-limitation were quantified to elucidate the interplay between multiphase mass transport and heat transport on the hydrate recovery efficiency. The regime diagram of the methane hydrate dissociation was mapped to exhibit five dissociation regimes according to the connate water saturation and the Péclet number. Empirical correction of the permeability and the specific surface area was obtained to improve the REV (Representative Element Volume)-scaled modeling accuracy of the volume-averaged transport and geometric properties with three typical dissociation patterns. The insights from the pore-scale multiphase dissociation studies can enlighten the accurate REV-scaled simulation with the addressed non-negligible physics.

Keywords: methane hydrate, multiphase flow, heat and mass transfer, pore-scale simulation, lattice Boltzmann method

1. Introduction

The methane hydrate is a crystalline compound containing the methane gas molecules hosted in the hydrogen-bonded water lattices by the intermolecular forces [1, 2]. Methane hydrate is widely distributed in the deep marine sediment and terrestrial permafrost worldwide [3, 4] under suitable conditions of low temperature and high pressure. Due to its high gas storage capacity and substantial reserves [5], methane hydrate is considered as the promising future energy and attracts significant attention from the world [6-9]. The various methods have been proposed for methane hydrate mining from the hydrate-bearing reservoirs in recent years, including thermal stimulation [10], depressurization [11], inhibitor injection [12], and the combination of these methods. These methods are associated with hydrate dissociation by breaking the thermodynamic equilibrium of the methane hydrate in the reservoir conditions. Some field tests have been carried out to investigate the technical feasibility of methane hydrate exploitation in recent years [7]. However, methane production is still limited due to the potential geohazard risk and the complex changes of thermodynamic and transport properties within the reservoir. Therefore, a better understating of the methane hydrate dissociation mechanism in the reservoir sediment is necessary to predict the production behavior, design the well arrangement plan and optimize the exploitation technique.

Methane hydrate dissociation in the reservoir sediment is a typical multi-physics problem involving multiphase flow, heat and mass transfer, dissociation chemical reaction and the solid structure evolution in the complex porous media [13]. During the dissociation process, the temperature decreases due to the endothermic dissociation

reaction. Meanwhile, the pressure increases as the methane gas is released. As the dissociation progresses, phase distributions of the solid methane hydrate, liquid water and gaseous methane evolve all the time, leading to the change of multiphase flow pattern and the formation permeability. The multiphase flow characteristics are critical in heat and mass transport, which significantly influences the temperature and pressure change [14]. These physical processes are fully coupled and bring complexity to understand the methane hydrate process comprehensively.

In recent years, numerous experimental and numerical studies have investigated the methane hydrate dissociation process from the laboratory to the field. As for the field-scale research, the field test data could evaluate the exploitation feasibility among different reservoir conditions, and field-scale numerical simulations were implemented for production forecasts and program optimization [8, 15, 16]. Due to the limited number of the field tests and the lack of knowledge on the volume-averaged transport, geometrical and kinetic properties for the field-scale numerical models, the lab-scale experiments [17-20] and simulation [21, 22] were introduced to elucidate the effect of the operation methods and reservoir condition on the hydrate dissociation process. Most of the lab-scale simulations are based on averaged properties within represented element volume (REV), but the physical knowledge to derive the volume-averaged transport, geometrical and kinetic properties still lack because detailed multi-physics processes and phase behavior within the sediment are challenging to observe in the lab-scale experiments. Therefore, these numerical simulations need the assistance of the history matching tool to reproduce the experimental results from the perspective of

mathematical optimization [23] although these lab-scale investigations escape the uncertainty of the geoelectrical structure and the complexity of the wells configuration in field-scale. Moreover, the effect of complicated pore structure evolution, phase behavior, and reaction nonlinearity of the methane hydrate dissociation process is always filtered in the REV models, which may introduce significant inaccuracy [24]. Therefore, pore-scale studies are necessary to understand the controlling mechanisms of the methane hydrate dissociation process in the sediment and provide more accurate kinetic and transport parameters for the REV models in field or lab scales.

As for the pore-scale experimental studies, the microfluidic technique [25-29] and microscopic X-ray computed tomography (micro-CT) [30-33] have been widely used to observe the hydrate distribution behaviors within the porous media from the perspective of 2-D and 3-D. Besides the morphological observation, several experimental attempts have also been conducted to investigate the physical and chemical mechanisms during the hydrate dissociation. Almenningen et al. [34] obtained hydrate phase equilibria during the microfluidic experiments and discussed the effect of heat transfer on the dissociation pattern [28]. Yang et al. [33] investigated hydrate dissociation with the synchrotron CT and found the methane molecule mass transfer in the water layer limited the dissociation rate, namely mass-transfer-limitation. These experimental analyses demonstrate that the heat and mass transfer mechanisms significantly impact the dissociation dynamics during the multiphase reactive flow in the porous media. However, since these visualization experiments are challenging to observe in detail the evolution of the concentration and temperature field, how the heat

and mass transfer mechanisms influence the dissociation performance cannot be determined quantitively. Due to the limited phenomena observed in the experiment, pore-scale numerical research is essential to quantitatively analyze the influence of different mechanisms, and then correct the volume-averaged properties for REV-scale models.

The pore-scale numerical model is challenging to comprehensively model the complicated hydrate dissociation, which couples the multiphase flow, heat and mass transport, chemical reaction and hydrate structure evolution within the complex pore structures. Zhang et al. [35] simulated the methane hydrate dissociation process considering single-phase flow. They found the temperature decrease resulting from the heat transfer mechanism limited the dissociation rate significantly and evaluated the permeability relation as a function of the hydrate saturation in idealized porous media. However, as the single-phase flow assumptions in their work ignored the mass-transfer limitation of the water layer, the effect of the multiphase mass transport mechanism was not well characterized. Wang et al. [14, 36] investigated ice formation and mass transfer limitation on the dissociation process in the pore structure. Their model considered heat and mass transfer with phase change comprehensively. Still, the interfacial transport phenomena and hydrate structure evolution could not be visually represented with the phase distribution computed by the saturation. For improvement, our previous work [24] established the pore-scale numerical model to simulate methane hydrate dissociation in the multiphase system. The numerical study achieved a satisfactory agreement on the residual hydrate profile by comparing numerical simulations and experiments,

emphasized the role of mass-transfer limitation on the hydrate dissociation, and eventually obtained a corrected model of the kinetic parameters for the REV-scale model. However, as the simulation was conducted in the closed system with the single pore structure, the effect of convective transportation on the concentration and temperature distribution was not considered. The volume-averaged parameters of the sediment porous media, including the permeability and surface area change, were also not available. The competitive limitation effect of mass transfer and heat transfer was not well quantified. Therefore, more comprehensive investigations are still needed on the heat and mass transport mechanisms coupled with the multiphase fluid flow within the complex hydrate-bearing porous media.

As mentioned in the previous work [24], the lattice Boltzmann method (LBM) has the solid capacity for pore-scale multi-physics problems, which benefits from its high computational efficiency [37] and abundant numerical models for multiphase flow with heat and mass transport [38, 39]. In the present study, a pore-scale numerical model based on LBM was developed to simulate the hydrate dissociation with low-methane-concentration gas injection in the hydrate sediment, considering the multiphase flow, heat and mass transfer, heterogeneous reaction, and hydrate structure evolution. Different heat and mass transport mechanisms with various water saturation were investigated to recognize their effect on the dissociation dynamics. According to the initial water saturation and the Péclet number, the regime diagram of the hydrate dissociation was given to present five dissociation regimes with the varying dissociation mechanisms. The permeability and specific surface area development were

analyzed to derive the REV-scale models of the transport and geometrical properties for the variable dissociation patterns. Since the numerical model was improved compared with the previous pore-scale studies for the single-phase system [35] or closed system [24], the present work can provide a more comprehensive understanding of the methane hydrate dissociation in the sediment.

2. Numerical Method

2.1 Physical Problem

The multiple physicochemical processes during methane hydrate dissociation can be schematically described in Figure 1 [24]. Initially, the methane hydrate exists stably with water and gas in the phase equilibrium state. When the hydrate phase equilibrium is broken with the decreasing methane partial pressure (concentration), the dissociation reaction occurs at the methane hydrate surface [40]. The evolution of the hydrate structure and the production of the water and methane impacts the multiphase flow in the sediment. The reactive transport mechanism then evolves the methane concentration considering the multiphase convection and interfacial molecule diffusion across the water and gas. Since the dissociation reaction is endothermic, the sediment temperature gradually decreases with conjugate heat transfer through different phases. The development of the local methane concentration and temperature in turn influence the hydrate dissociate rate. Therefore, the multiphase flow, heat and mass transfer, and hydrate structural evolution are fully coupled with the hydrate dissociation reaction.

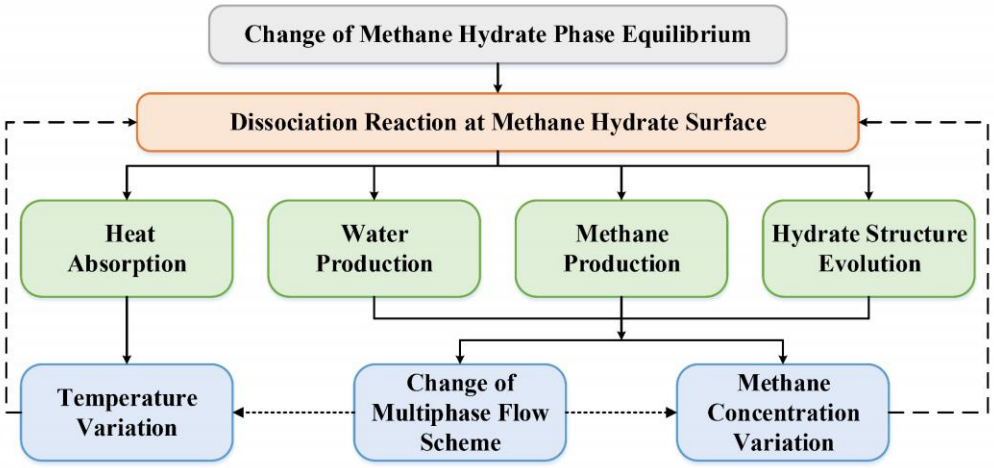

Figure 1 Schematic description of methane hydrate dissociation process with multiple mechanisms.

The following simplifications and assumptions are made to construct the governing equations to model the hydrate dissociation process: (1) The methane can be dissolved in the water as a dilute solution, and the gas phase is regarded as the ideal gas. (2) The methane molecules can diffuse across the water and gas phase following Fick's law, and the methane concentration distribution at the gas-water interface can be determined by Henry's law. (3) The dissociation reaction only occurs at the hydrate surface, while the hydrate reformation and ice formation are neglected. When the temperature decreases to 273.15 K, the dissociation is numerically stopped to take the inhibitory effect of ice formation into account. (4) The effect of heat transfer and methane transfer on the fluid flow can be neglected so that the multiphase flow can be one-way coupled with the heat and species advection-diffusion. The non-slip boundary condition is enforced at the solid surface, and the buoyancy force is negligible. (5) Since the temperature change in the sediment is not dramatic (lower than 15 K), the physical properties of the fluid and hydrate are treated as constant. Based on the above

assumptions, the governing equations of the fluid flow, methane transport, and heat transfer can be described as

$$\begin{aligned}&\frac{\partial \rho}{\partial t}+\nabla\cdot\left(\rho\mathbf{u}\right)=0\\&\frac{\partial\left(\rho\mathbf{u}\right)}{\partial t}+\nabla\cdot\left(\rho\mathbf{u}\mathbf{u}\right)=-\nabla p+\nabla\cdot\left(\rho\upsilon\left(\nabla\mathbf{u}+\left(\nabla\mathbf{u}\right)^{T}\right)\right)+\nabla\left(\rho\xi\left(\nabla\cdot\mathbf{u}\right)\right)\end{aligned}\tag{1}$$

$$\frac{\partial C}{\partial t}+\nabla\cdot\left(C\mathbf{u}\right)=D\nabla^{2}C \tag{2}$$

$$\rho c_{p}\frac{\partial T}{\partial t}+\nabla\cdot\left(\rho c_{p}T\mathbf{u}\right)=\nabla\cdot\left(\lambda\nabla T\right)+S_{H} \tag{3}$$

where ρ and $\mathbf{u}$ are fluid density and velocity, C is the methane concentration, and T is the temperature. ξ is dynamic viscosity, D is the diffusivity of the methane molecule, λ is the conductivity, and c_p is the specific heat capacity. The dissociation reaction on the methane hydrate surface can be modeled as [35]

$$\mathrm{CH_4}\cdot n_{\mathrm{H}}\mathrm{H_2O}\rightarrow\mathrm{CH_4}+n_{\mathrm{H}}\mathrm{H_2O} \tag{4}$$

where n_{H} is the hydrate number and was set as $n_{\mathrm{H}}=6$. As our previous work [24], the Kim-Bishnoi model [40] was used to compute the dissociation rate as

$$\frac{dn_{\mathrm{CH_4}}}{dt}=k_0\exp\left(\frac{E_A}{RT}\right)\left(f_{\mathrm{eq}}-f\right)A_{\mathrm{s}} \tag{5}$$

where E_A is the activation energy, k_0 is the pre-exponential factor, and A_{s} denotes the surface area. In the present work, the fugacity f was computed by the methane concentration based on the assumption that the gas phase is ideal and the water phase can be regarded as the dilute solution; therefore, the reaction kinetics can be calculated by

$$\frac{dn_{\mathrm{CH_4}}}{dt}=k_{C0}\exp\left(\frac{E_A}{RT}\right)\left(C_{\mathrm{eq,\,g}}-C_{\mathrm{g}}\right)A_{\mathrm{s}}=\frac{1}{H}k_{C0}\exp\left(\frac{E_A}{RT}\right)\left(C_{\mathrm{eq,\,w}}-C_{\mathrm{w}}\right)A_{\mathrm{s}} \tag{6}$$

where C_{w} and C_{g} represent the methane concentration in the water and gas phase with the relationship of $C_{\mathrm{w}} = HC_{\mathrm{g}}$ by Henry's law. The equilibrium concentration can be obtained by the Kamath model as [41, 42]

$$C_{\mathrm{eq,\,g}} = \frac{p_{\mathrm{eq,\,g}}}{ZRT} = \frac{1}{ZRT}\exp\left(38.980 - \frac{8533.80}{T}\right),\ 273.15\ \mathrm{K} < T \le 298.15\ \mathrm{K} \tag{7}$$

where Z is the coefficient of compressibility in the state equation $p = n(ZRT)/V = C(ZRT)$ and set as Z =0.83 in the present work. The reaction boundary condition on the hydrate surface can be written as

$$D\left.\frac{\partial C}{\partial n}\right|_{\mathrm{h}} = -k_{C0}\exp\left(\frac{E_A}{RT}\right)\left(C_{\mathrm{eq,\,g}} - C_{\mathrm{g}}\right)_{\mathrm{h}} = -k_C\left(C_{\mathrm{eq,\,g}} - C_{\mathrm{g}}\right)_{\mathrm{h}} \tag{8}$$

and the reaction heat source can be calculated as

$$S_H = k_C\left(C_{\mathrm{eq,\,g}} - C_{\mathrm{g}}\right)_{\mathrm{h}}\Delta H \tag{9}$$

where ΔH is the reaction enthalpy.

The methane hydrate distribution in the reservoir sediment is complicated. The laboratory observation identified various hydrate distributions, including grain-coating, pore-filling, bridging and matrix-supporting [43, 44]. The typical hydrate distributions comprising pore-filling (hydrate occupies pore centers) and grain-coating (hydrate coats the sediment matrix) were commonly used to analyze the effect of the hydrate sediment structures on the permeability in previous pore-scale studies [45-47]. In contrast to the permeability analyses, this work introduced a 2-D idealized porous structure with the typical grain-coating hydrate pore habit for a general understanding of the hydrate dissociation physics without respect to the complicated porous structures, as shown in Figure 2. Black pixels represent the rock matrix, and gray pixels denote the

methane hydrate. The total computational domain is 12 mm in length and 3 mm in width, meshed with a 1200×300 lattice grid. The porosity of the rock matrix is ϕ=0.649, and the initial hydrate saturation is $S_{\mathrm{hyd}}=0.324$. At the beginning of the simulation, the water, methane, and hydrate coexist in equilibrium at the temperature of 288.15 K, which is similar to the representative submarine reservoir condition. According to the hydrate equilibrium line described by Eq. (7), the pressure within the sediment is 11.5 MPa, corresponding to the methane concentration of 5.75 mol/L in the gas phase. Then, the inert gas is injected from the left inlet at a certain velocity with the methane concentration $C_{\mathrm{in,CH_4}}=0$ mol/L. The total pressure in the sediment changed slightly since the pressure difference between the inlet and outlet was small ($\Delta p=0.33$ Pa when Péclet number Pe=2.5), but the methane concentration continuously dropped due to the intrusion of the inert gas. After that, the phase equilibrium was broken, and the dissociation started with the reaction rate determined by Eq. (8). The physical properties used in the numerical models are listed in Table 1.

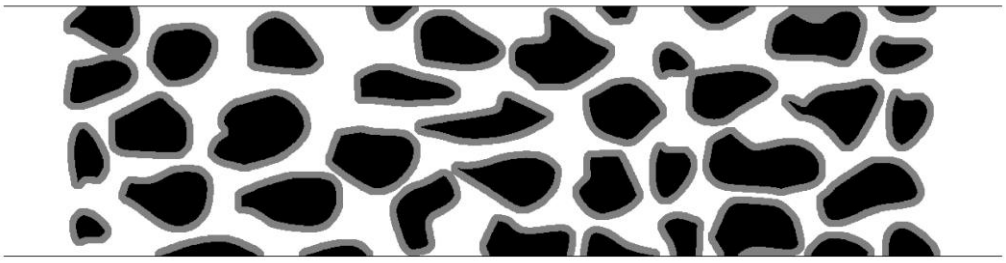

Figure 2 Computational domain for methane hydrate dissociation simulation. The gray color represents the hydrate, and the black color represents the sediment matrix. The gas and water flowed in the pore structure.

Table 1 Physical properties for the simulation

Water density, ρ_{w}	1000 kg/m^3
Gas density, ρ_{g}	100 kg/m^3
Initial temperature, T_0	288.15 K
Initial concentration in gas phase, C_{g0}	5.75 mol/L
Henry coefficient, H	0.5
Kinematic viscosity of water, υ_{w}	1.0×10^{-6} m^2/s
Kinematic viscosity of gas, υ_{g}	1.57×10^{-5} m^2/s
Methane diffusivity in water, D_{w}	5×10^{-7} m^2/s
Methane diffusivity in gas, D_{g}	2.4×10^{-5} m^2/s
Pre-exponential factor, k_{C0}	5.13×10^{9} m/s
Activation energy, E_A / R	9399 K
Reaction heat, ΔH	51.86 kJ/mol
Thermal conductivity of water, λ_{w}	0.55 W/(m·K)
Thermal conductivity of gas, λ_{g}	0.045 W/(m·K)
Thermal conductivity of solid, λ_{s}	0.49 W/(m·K)
Specific heat capacity of water, $c_{p\mathrm{w}}$	4.2 kJ/(kg·K)
Specific heat capacity of gas, $c_{p\mathrm{g}}$	3.2 kJ/(kg·K)
Specific heat capacity of solid, $c_{p\mathrm{s}}$	2.1×10^{3} kJ/(m^3·K)

2.2 Numerical Models

Lattice Boltzmann method [48] was used to solve the above governing equations in the present study. The numerical implementations of the LB models are introduced briefly in this section. More details can be found in the previous work [24, 49].

2.2.1 Multiphase flow model

The pseudopotential multiphase LB model [50] was adopted to simulate the water-gas multicomponent multiphase flow. The multiple-relation-time (MRT) collision operator was introduced to reduce the spurious current and improve the computational stability [51]. The LB equation for the σth component with force term can be expressed as

$$\mathbf{f}^{\sigma}(\mathbf{x}+\mathbf{c}_i\Delta t, t+\Delta t)-\mathbf{f}^{\sigma}(\mathbf{x},t)=-\mathbf{M}^{-1}\mathbf{S}^{\sigma}\left[\mathbf{m}^{\sigma}(\mathbf{x},t)-\mathbf{m}^{\sigma,\mathrm{eq}}(\mathbf{x},t)\right]+\Delta t\cdot\mathbf{M}^{-1}\left(\mathbf{I}-\frac{\mathbf{S}^{\sigma}}{2}\right)\mathbf{F}^{\sigma}+\mathbf{w}S_M^{\sigma} \tag{10}$$

where $\mathbf{m}^{\sigma}=\mathbf{M}\mathbf{f}^{\sigma}$ is the moment of the density distribution function, and $\mathbf{S}^{\sigma}$ is the diagonal relaxation matrix involving the relaxation parameters determined by the fluid viscosity. $\mathbf{F}^{\sigma}$ is the force term and S_M^{σ} is the mass source term due to the hydrate dissociation. This numerical model Eq. (10) can be derived into Navier-Stokes equation Eq. (1) with Chapman-Enskog analysis. In the conventional pseudopotential model, the intracomponent and intercomponent force schemes are usually combined to realize phase separation with a high-density ratio [52]. However, the combination of these two forces brings high spurious current. The spurious current caused the unphysical species mass flux in the mass transfer computation. Since the methane diffusivity in the water phase was low, this unphysical mass flux could dominant the diffusion mass flux, leading to the inaccuracy of the mass transfer simulations. Therefore, in the present study, only intercomponent force $\mathbf{F}_{\sigma\bar{\sigma}}$ [53] in Eq. (11) was introduced. The water-gas density ratio was set as $\rho_{\mathrm{w}}/\rho_{\mathrm{g}}=1$ after weighing the spurious current against the numerical accuracy.

$$\mathbf{F}_{\sigma\bar{\sigma}} = -G_{\sigma\bar{\sigma}}\varphi_{\sigma}(\mathbf{x})\sum_{\alpha} w\left(|\mathbf{e}_{\alpha}|^2\right)\varphi_{\bar{\sigma}}(\mathbf{x}+\mathbf{e}_{\alpha})\mathbf{e}_{\alpha},\ \varphi_{\sigma}(\rho_{\sigma}) = 1-\exp(-\rho_{\sigma}/\rho_{\sigma 0}) \tag{11}$$

where φ_{σ} is the pseudopotential and $\mathbf{e}_{\alpha}$ is the discrete velocities of LBM. This treatment set the water density $\rho_{\mathrm{w}} = 100$ kg/m^3, which might bring some deviation of the multiphase flow from the natural process. However, as the heat and mass transfer mechanisms are the central focus of the present study rather than the multiphase flow patterns, the propagation deviation to the heat and mass transfer in the current porous structure can be acceptable and less impacted to the primary conclusion. Additionally, the water thermophysical properties, such as the specific heat capacity, were also adjusted to guarantee that the Prandtl number $\mathrm{Pr} = \rho\upsilon c_p / \lambda$ and Schmidt number $\mathrm{Sc} = \upsilon / D$ remained natural physical properties and reproduced the competitive strength of different heat and mass transfer mechanisms. The validation of the multiphase flow LB model has been carried out in our previous work [24] and the improvement of the numerical model to realize the hydrate dissociation within the high-density-ratio multiphase system will be conducted in future work.

2.2.2 Mass transfer model

When simulating the mass transfer process in the multiphase system, the interfacial species transport enforced by Henry's law should be handled with care. In this work, the CST (Continuum Species Transfer)-LB model [49] with D2Q5 scheme (the discrete velocity vectors in the diagonal directions are abandoned without accuracy loss [54]) is used to describe the interfacial transport of methane molecules as

$$
\begin{aligned}
&g_\alpha(\mathbf{x}+\mathbf{e}_\alpha\Delta t, t+\Delta t)-g_\alpha(\mathbf{x},t)=-\frac{1}{\tau_D}[g_\alpha(\mathbf{x},t)-g_\alpha^{\mathrm{eq}}(\mathbf{x},t)]+\Omega_{\mathrm{CST},\alpha}\\
&\Omega_{\mathrm{CST},\alpha}=\left(1-\frac{1}{2\tau_D}\right)J_\alpha C\frac{H-1}{Hx_{\mathrm{w}}+(1-x_{\mathrm{w}})}\left(\mathbf{e}_\alpha\cdot\nabla x_{\mathrm{w}}\right)\Delta t
\end{aligned}
\tag{12}
$$

where g_α is the concentration distribution function and τ_D is the relaxation time. The effective diffusion coefficient and the total concentration can be calculated with water phase fraction $x_{\mathrm{w}}=\varphi_{\mathrm{w}}/\left(\varphi_{\mathrm{w}}+\varphi_{\mathrm{g}}\right)$ by

$$
\begin{aligned}
&D=\frac{D_{\mathrm{w}}D_{\mathrm{g}}}{x_{\mathrm{w}}D_{\mathrm{w}}+(1-x_{\mathrm{w}})D_{\mathrm{g}}}=\frac{1}{2}\left(1-J_0\right)\left(\tau_D-0.5\right)\frac{\Delta x^2}{\Delta t}\\
&C=x_{\mathrm{w}}C_{\mathrm{w}}+\left(1-x_{\mathrm{w}}\right)C_{\mathrm{g}}=\sum_\alpha g_\alpha
\end{aligned}
\tag{13}
$$

Using the Chapman-Enskog analysis, the CST-LB equation can recover the continuum species transfer equation proposed by Haroun et al [55].

$$
\begin{aligned}
&\frac{\partial C}{\partial t}+\nabla\cdot\left(\mathbf{u}C\right)=\nabla\cdot\left(D\left(\nabla C+\Phi_{\mathrm{CST}}\right)\right)\\
&\Phi_{\mathrm{CST}}=-\frac{C\left(H-1\right)}{Hx_{\mathrm{w}}+\left(1-x_{\mathrm{w}}\right)}\nabla x_{\mathrm{w}}
\end{aligned}
\tag{14}
$$

which can successfully treat the concentration jump at the phase interphase with the satisfying mass flux conservation. The dissociation reaction boundary condition is enforced as

$$
\mathbf{e}_\alpha g_\alpha(\mathbf{x},t)=-\mathbf{e}_{\bar{\alpha}}g_{\bar{\alpha}}^*(\mathbf{x},t)+k_{C0}\exp\left(\frac{E_A}{RT}\right)\left(C_{\mathrm{eq,\,g}}-C_{\mathrm{g}}\right)_{\mathrm{h}}
\tag{15}
$$

where g_α is the unknown concentration distribution function on the boundary grid and $g_{\bar{\alpha}}^*$ is the distribution function in the opposite direction of α after the collision step. The mass source term of water was also considered for the multiphase flow model Eq. (10), which is calculated by

$$
S_M^{\mathrm{w}}=k_{C0}\exp\left(\frac{E_A}{RT}\right)\left(C_{\mathrm{eq,\,g}}-C_{\mathrm{g}}\right)_{\mathrm{h}}\cdot MW_{\mathrm{w}}\cdot n_{\mathrm{H}}
\tag{16}
$$

More details and model validation of the CST-LB model can be found in our previous work [49].

2.2.3 Heat transfer Model

The double-distribution-function thermal LB model is employed to simulate the heat transfer process as [56]

$$h_\alpha(\mathbf{x}+\mathbf{e}_\alpha\Delta t, t+\Delta t)-h_\alpha(\mathbf{x},t)=-\frac{1}{\tau_\chi}[h_\alpha(\mathbf{x},t)-h_\alpha^{\mathrm{eq}}(\mathbf{x},t)]+J_\alpha S_c\Delta t+J_\alpha S_h\Delta t \tag{17}$$

where h_α is the temperature distribution function and τ_χ is the relaxation time related to the thermal diffusivity $\chi=\lambda/\rho c_p$. S_h is the reaction heat source term and S_c is the conjugate source term to model the conjugate heat transfer by [57]

$$S_c=\nabla\left(\frac{1}{\rho c_p}\right)\cdot\left(-\lambda\nabla T+\rho c_p T\mathbf{u}\right) \tag{18}$$

Based on Chapman-Enskog analysis, the above LB equation can recover the energy equation Eq. (3). The heat transfer model has been verified in our previous work [24].

2.2.4 Update of solid phase

The VOP (volume of the pixel) method proposed by Kang et al. [58] is adopted to track the evolution of the hydrate structure. Initially, the hydrate volume is set as zero within the fluid cell and one within the hydrate cell. When the dissociation reaction starts, the hydrate volume within each hydrate cell is updated by

$$V_{\mathrm{hdy}}(t+\Delta t)=V_{\mathrm{hdy}}(t)-k_{C0}\exp\left(\frac{E_A}{RT}\right)\left(C_{\mathrm{eq,g}}-C_{\mathrm{g}}\right)_{\mathrm{h}}V_M A_{\mathrm{s}}\Delta t \tag{19}$$

where V_M is the molar volume of the methane hydrate. When V_{hyd} declined to zero, the hydrate node is converted to the fluid node. The physical information at this

converted node was updated by averaging over the neighboring fluid nodes, including the water density, gas density, velocity and methane concentration.

2.3 Numerical Procedure

Figure 3 shows the numerical procedure to simulate the reactive transport and thermal process during the methane hydrate dissociation. The numerical implementations were in-house developed with C++ language, and the validation of the numerical models has been carefully conducted [24, 49].

The main implementation steps are:

1. Simulate the water-gas fluid flow using the multiphase flow model (Eq. (10)) to update the water phase fraction x_{w} and fluid velocity $\mathbf{u}$.

2. Compute the effective diffusivity by Eq. (14) and solve the methane concentration distribution C with the mass transfer model (Eq. (12)). Calculate the mass source term and heat source term of the dissociation reaction.

3. Compute the fluid thermal diffusivity with the water phase fraction $\chi = \chi_{\mathrm{w}}\chi_{\mathrm{g}} / \left(x_{\mathrm{w}}\chi_{\mathrm{w}} + (1-x_{\mathrm{w}})\chi_{\mathrm{g}} \right)$. Simulate the conjugate heat transfer using the heat transfer model (Eq. (17)) to obtain the temperature distribution T.

4. Update the solid hydrate phase using the VOP method (Eq. (19)) and initialize the properties at the newly generated fluid cells.

5. Compute the methane concentration in the gas phase $C_{\mathrm{g}} = C / \left(Hx_{\mathrm{w}} + 1 - x_{\mathrm{w}} \right)$ and update the hydrate dissociation reaction kinetics and equilibrium concentration.

6. Repeat steps 1-5 till the completion of the methane hydrate dissociation.

To verify the reliability of the numerical procedure, the numerical simulation

based on the experimental image from Yang et al. [33] was carried out in the appendix.

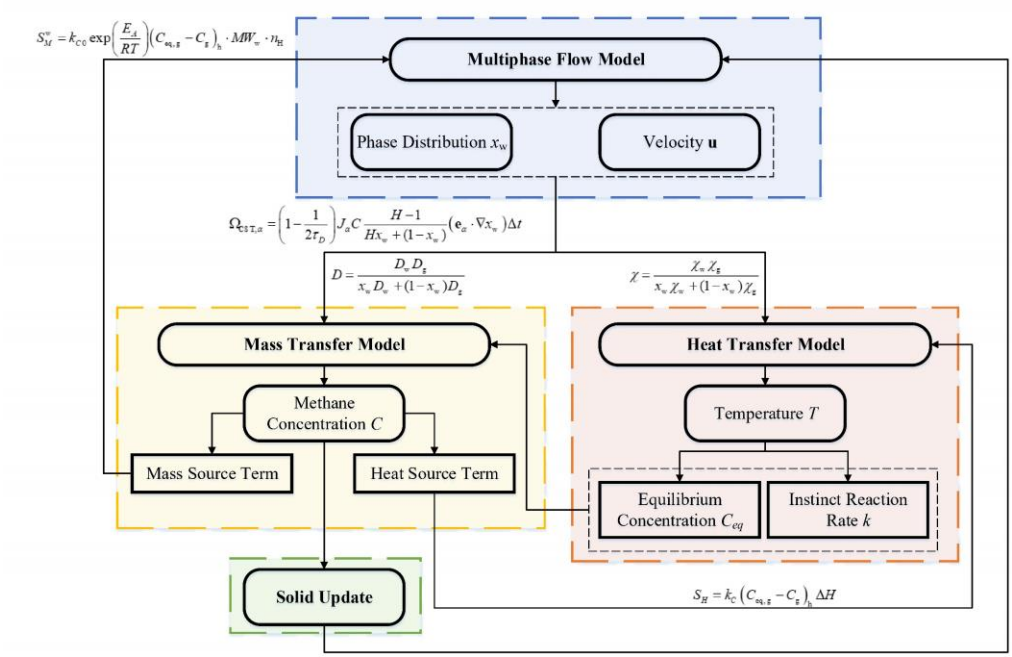

Figure 3 Schematic diagram of the numerical implementation.

At the beginning of the simulation, an artificial water-gas distribution with the prescribed initial water saturation was first given to the computational domain. Then, the multiphase flow model was computed without heat and mass transport until the steady-state to yield the physical phase distributions with different water saturation, as shown in Figure 4. During the phase separation computation, the inlet and outlet were temporarily set as the non-slip wall boundary, and the solid matrix and hydrate phase were set hydrophilic by adjusting the static contact angle as $\theta_{\mathrm{wg}} = 20^{\circ}$. Hereafter, the numerical procedure mentioned in Sect. 2.3 was started to simulate the hydrate dissociation process. The inlet methane concentration and temperature were set as 0 mol/L and 288.15 K, respectively.

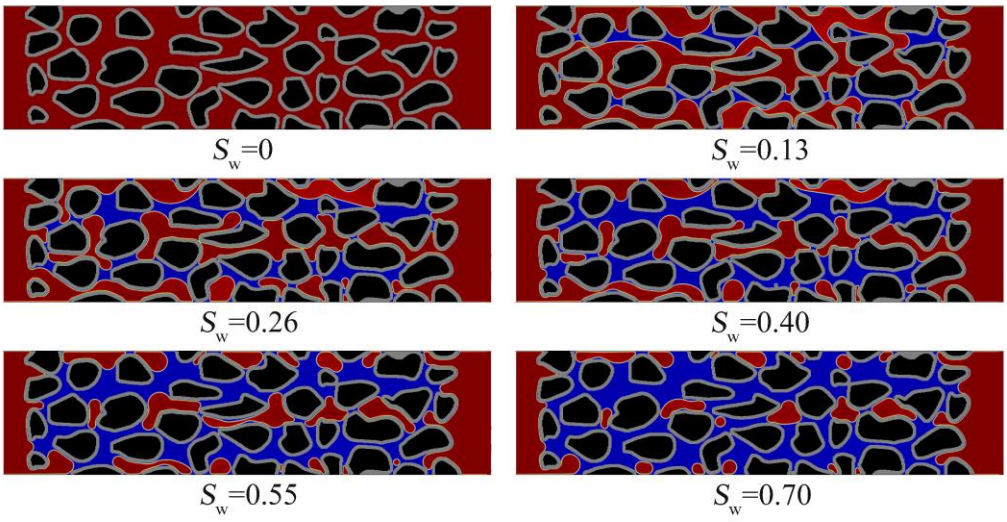

Figure 4 Initial gas-water distribution with different water saturation for multiphase heat and mass transport simulation of methane hydrate dissociation process. The red color represents the gas, and the blue color denotes the water. The gray and black colors are methane hydrate and sediment matrix, respectively.

3. Results and Discussion

The single-phase hydrate dissociation was first investigated to understand the regime boundaries of convection and diffusion transport-limited processes. The multiphase dissociation was then analyzed to determine the effect of water saturation on the dissociation dynamics and competitive dissociation limitation mechanism at the convection and diffusion transport-limited regimes, respectively. Later, the phase diagram of the hydrate dissociation with five representative dissociation regimes was exhibited to summarize the critical mechanisms with various conditions. Eventually, empirical corrections of the volume-averaged transport property, gas permeability, and the geometric property, the hydrate surface area were proposed to improve the REV-scaled modeling accuracy by taking the different hydrate dissociation patterns into account.

3.1 Dissociation pattern and controlling mechanism of single-phase hydrate dissociation

Methane hydrate dissociation with different gas injection rates was first investigated to understand the effect of convection strengths of heat and mass transport on the dissociation rate, which can be quantified by the Péclet number as

$$\mathrm{Pe} = \frac{UL}{D} \tag{20}$$

where U is the Darcy velocity, D is the methane diffusivity in the gas phase, and L is the characteristic length set as the mean grain size of the sediment 600 μm. The range of Pe number from $\mathrm{O}\left(10^{-4}\right)$ to $\mathrm{O}\left(10^{0}\right)$ was covered in the simulation, and their temporal evolutions of the hydrate saturation are compared in Figure 5. The dissociation rates with low gas flow rates (Pe=0.00025 and Pe=0.0025) were almost coincident, indicating the increasing fluid velocity had an ignorance effect on the dissociation rate when the Pe number was less than $\mathrm{O}\left(10^{-2}\right)$. When Pe number was higher than $\mathrm{O}\left(10^{-2}\right)$, the dissociation rate increased significantly with the fluid velocity (Pe=0.25, Pe=2.5), indicating the fluid flow velocity became vital to the hydrate dissociation within this Pe range. For a more intuitive understanding of the evolution characteristics during the hydrate dissociation, the methane concentration and temperature field of two typical Pe cases (low Pe of 0.0025 and high Pe of 0.25) at different time instants are illustrated in Figure 6 and Figure 7.

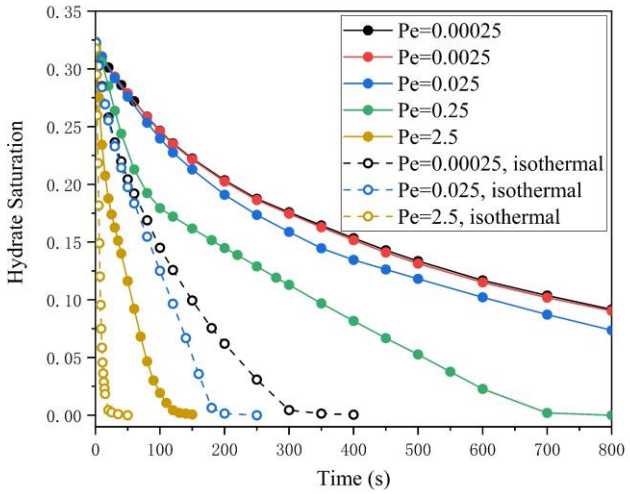

Figure 5 Temporal evolution of the hydrate saturation for different Pe cases. Dash lines with hollow markers represent the isothermal dissociation process without considering the heat transfer.

As shown in Figure 6 for the low fluid velocity case of Pe=0.0025, the injected inert gas flowed into the channel from the left inlet, resulting in the methane concentration drop near the entrance and triggered the methane hydrate dissociation. The profile of the dissociation front is characterized in the temperature contour maps in Figure 6. It can be found the dissociation front advanced slowly in parallel and the shape is perpendicular to the direction of injection flow, which can be identified as 'facial dissociation pattern'. As observations, the methane concentration field presented a typically diffusion-driven scheme at t=100 s, implying that the diffusion mechanism was dominant over convective transport. Besides the methane convection, the effect of the dissociation reaction on the concentration evolution was also negligible as the Damköhler number defined by Eq. (21) was relatively small. The Da number was only 0.085 at 288.15 K, and further declined with the decreasing temperature due to the

endothermic nature of the hydrate dissociation. Therefore, diffusion transport dominated the propagation of the methane concentration for the low Pe cases in the single-phase situation.

$$\mathrm{Da} = \frac{k_C L}{D} \tag{21}$$

As for the heat transfer, the temperature decreased to 273.15 K at the dissociation front due to the reaction endotherm and suppressed the hydrate dissociation. To quantify the competitive strength of reaction endotherm over the conductive heat transport, the thermal Da number is defined as

$$\mathrm{Da}_T = \frac{k_C L \Delta H \Delta C}{\lambda \Delta T} \tag{22}$$

where ΔT was set as the maximum temperature difference 15 K and ΔC was specified as $\Delta C = C_{\mathrm{eq}} - C_{\mathrm{in}} = 5.75$ mol/L . The thermal Da number was high ($\mathrm{Da}_T = 9.14$ at 288.15 K) even though the temperature decreased to a low level ($\mathrm{Da}_T = 2.82$ at 278.15 K), indicating the reaction heat absorption was dominant in the temperature evolution. As the dissociation proceeded, the methane concentration inside the whole domain dropped and maintained close to the inlet concentration (when *t*=500 s in Figure 6), suggesting that the temperature developed into the crucial factor limiting the dissociation rate. To highlight the effect of temperature, the isothermal hydrate dissociation without reaction endotherm was simulated at different Pe numbers with the results also illustrated in Figure 5. It can be seen that the methane hydrate dissociation rate was falsely accelerated when the reaction endotherm was not considered. For Pe=0.025, the hydrate only spent 200 s to be consumed entirely under isothermal conditions. In comparison, the hydrate dissociation should sustain for 1200 s when

considering the reaction endotherm, indicating the decreasing temperature significantly delayed the hydrate dissociation, which was regarded as the heat-transfer-limitation. The present study introduced the heat-transfer-limitation concept to measure how much the dissociation efficiency reduced from the intrinsic rate at the initial temperature when taking the dissociation endotherm and the subsequent heat transport into account.

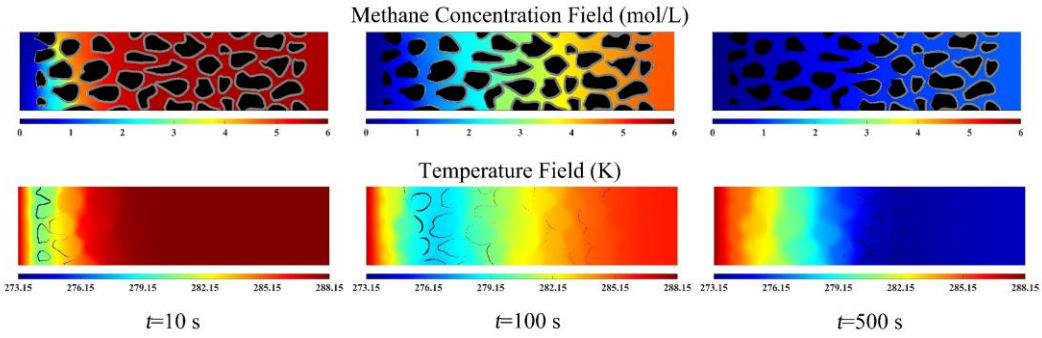

Figure 6 The temporal evolution of the methane concentration (top) and temperature (bottom) during the methane hydrate dissociation with single-phase gas flow under the low Pe condition of Pe=0.0025. The gray and black colors in methane concentration contours indicate the hydrate and sediment matrix, respectively. The gray/black lines in the temperature contour denote the dissociation front where the dissociation reaction occurred, and the grayscale reflects the dissociation rate.

For the high Pe case of Pe=0.25, as shown in Figure 7, the methane concentration presented the different evolution characteristics where the convection transport became prominent. The dissociation rate increased significantly with the gas flow rate, as shown in Figure 5. As the pore structure had the preferential flow region, the methane concentration decreased rapidly in local with the high fluid velocity but spread slowly to other pore spaces through molecule diffusion, as shown in Figure 7 when t=30 s. As a result, the methane hydrate dissolved faster in the preferential flow region than the

low-velocity regions, leading to the heterogeneity of hydrate structure evolution with a conical dissociation pattern. Although the thermal convection was enhanced, the temperature still decreased dramatically during the hydrate decomposition, indicating the dissociation endotherm was still the dominant mechanism over the convective and diffusive heat transport in the temperature evolution.

In summary, the methane concentration evolution depended on the competitive mechanism of methane convective and diffusive transport for the single-phase methane hydrate dissociation process. For high gas injection rates with $\mathrm{Pe} > \mathrm{O}\left(10^{-2}\right)$, increasing the fluid velocity can significantly improve the dissociation rate and represent a conical dissociation pattern. When the gas injection rate was low with $\mathrm{Pe} < \mathrm{O}\left(10^{-2}\right)$, the methane transport became dominated by slow diffusion. The dissociation rate was much slower than the high Pe conditions and showed a facial dissociation pattern. As to the temperature evolution, the reaction endotherm prevailed over the convective and conductive heat transport and remarkably inhibited the hydrate dissociation.

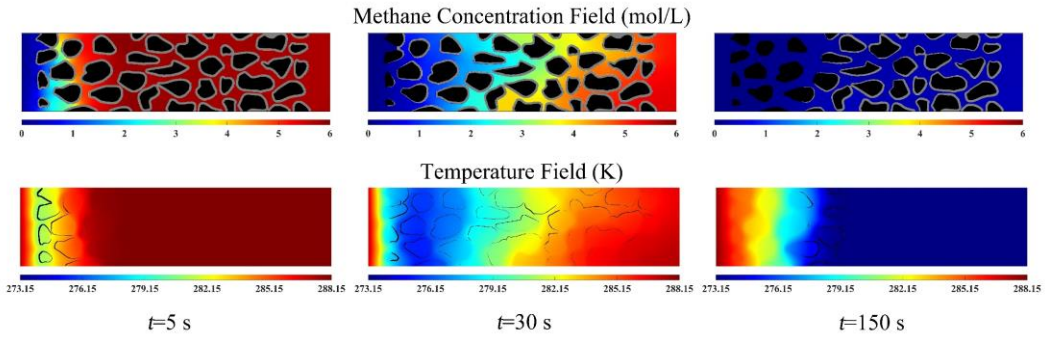

Figure 7 The temporal evolution of the methane concentration (top) and temperature (bottom) during the methane hydrate dissociation with single-phase gas flow under the high Pe condition of Pe=0.25.

3.2 Dissociation dynamics and competitive mechanisms of multiphase hydrate dissociation with different water saturation

Following the identification of distinctive convection and diffusion transport-limited regime through the single-phase dissociation simulation, the effect of connate water saturation on the multiphase dissociation were investigated with Pe=0.25, referred to hereafter as the high Pe condition, and Pe=0.0025, referred to hereafter as the low Pe condition. During the analysis for each Pe condition, the multiphase dissociation pattern was firstly distinguished according to temporal snapshots of dissociation dynamics. Secondly, the multiphase dissociation mechanism was clarified based on the methane concentration-temperature (*C*-*T*) trajectory in the hydrate phase diagram. Eventually, the dissociation limitation mechanism, consisting of the heat-transfer-limitation and mass-transfer-limitation, was quantitatively measured to reveal the effect of the water saturation on the hydrate dissociation rate.

3.2.1 High Pe condition

The methane hydrate dissociation with different initial water saturation with Pe=0.25 was simulated. Figure 8 shows the methane concentration and temperature evolution with a low initial water saturation of $S_w = 0.13$. Initially, the water was dispersed in the sediment, and the gas phase held a pre-existing continuous pathway throughout the computational domain. At this moment, the effect of the water distribution on methane transport was not noticeable. As expected, the methane concentration evolution in the gas phase at the early stage (*t*=5 s) was similar to the single-phase situation in Figure 7. When *t*=30 s, as the dissociation progressed, the

water was produced and formed the water layer covered on the hydrate surface at the dissociation front. Compared to the exposed hydrate to the gas, the hydrate in contact with the water layer dissolved slower since the low methane diffusion rate in water restricted the methane transportation. The hydrate dissociation rate decreased with the reduced dissociation fugacity difference at the water-hydrate interface, regarded as the mass-transfer-limitation [24]. Afterward, the low-methane-concentration gas entered the channel mainly through the preferential flow region, where the convective transport prevailed, leading to the decreasing methane concentration and paramount hydrate dissociation there. Meanwhile, the less mobile connate and produced water gradually developed into the flow barrier to prevent the displacement of the low-methane-concentration gas into other less permeable regions. Hereafter, some methane bubbles slowly grew and were encapsulated in the pore space, resulting in enriched methane inside the bubbles could not flow out of the domain. Instead, methane molecules should escape the trapped bubbles through the interfacial transport across the gas and water phase, subsequently mitigating the methane concentration evolution and thus maintaining the high methane concentration within bubble-trapped regions. Compared to the covered water layer, the intensified mass-transfer-limitation at the bubble-trapped regions further reduced the hydrate dissociation rate due to the locally imperceptible fugacity difference. What was worse, the temperature downstream uniformly decreased due to the remarkable endothermic dissociation at the neighboring preferential flow region and the subsequent heat conduction, as shown in Figure 8 (a) at t=150 s. As discussed in the single-phase situation, the low temperature close to 273.15 K further

inhibited the hydrate dissociation in the bubble-trapped region, referred to as heat-transfer-limitation. Therefore, the highly weakened hydrate dissociation dynamics in the bubble-trapped regions at t=150 s was attributed to both the mass-transfer-limitation and heat-transfer-limitation.

As the illustration of the profile of hydrate dissociation front accompanied with the temperature contour in Figure 8(a) at t=30 s, most of the dissociation fronts resided in the preferential region, leading to the heterogeneity of the hydrate structure evolution, referred to as the wormholing dissociation in the present study. The sediment could be divided into two regions from the spatial view: the preferential flow region and the bubble-trapped region, as labeled on water-gas distribution at t=150 s in Figure 8(b). From a temporal perspective, the strong convective transport in the preferential flow region favored the initial hydrate dissociation, resulting in the approximately high dissociation rate as the single-phase scenario. When the hydrate in the preferential flow region was almost melted away, the bubble-trapped region contributed to the hydrate dissociation, leading to the slowed-down dissociation rate in the typical multiphase system. More details into the temporal profile of hydrate saturation will be discussed in this section after the elucidation of underlying dissociation mechanisms. What should be commented here is despite the trapped bubbles surrounded by the water layer were universally observed during the hydrate dissociation by the previous experimental studies [26, 28, 33], their influence on the dissociation dynamics was not attracted sufficient attention. Based on the discussion above, the present pore-scale simulation provides more insights into the formation of the encapsulated bubbles and their impact

on the spatially heterogenous wormholing dissociation and the temporally varying dissociation rate.

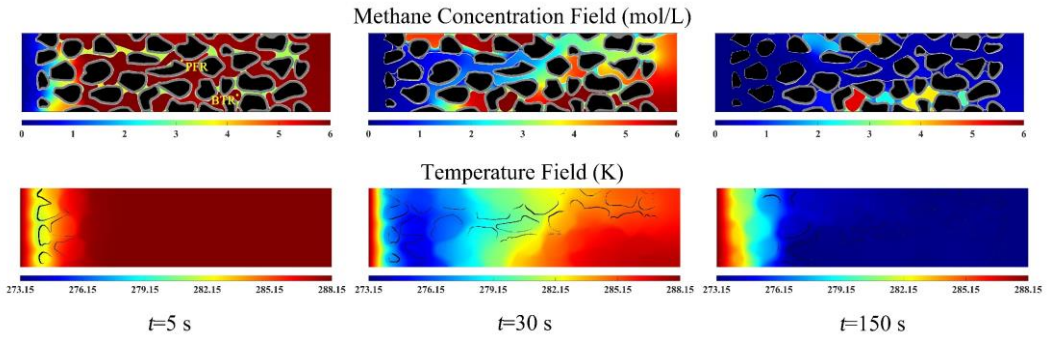

(a)

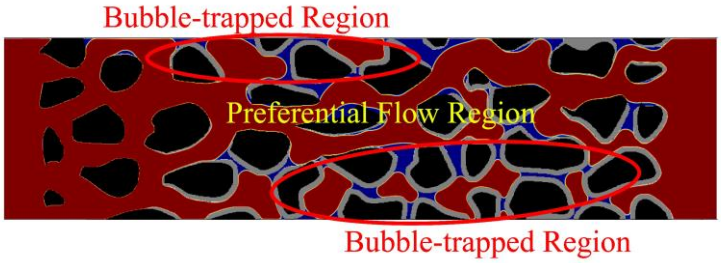

(b)

Figure 8 (a) The temporal evolution of the methane concentration (top) and temperature (bottom) during the methane hydrate dissociation with initial water saturation of $S_w = 0.13$ and the high Pe condition of Pe=0.25. (b) Water-gas distribution when t=150 s. The red color denotes the gas, and the blue color denotes water.

Figure 9 shows the hydrate dissociation dynamics with high initial water saturation of $S_w = 0.55$ and the high Pe number of Pe=0.25. The water phase occupied most of the pore space, and the gas phase existed as scattered bubbles without pre-existing interconnected pathways. At the beginning (t=5 s), the connate water blocked the injected low-methane-concentration gas and constrained the spread of the low methane

concentration as a result of the weak methane interphase diffusion. Due to the high gas injection velocity, the gas preferentially penetrated some regions and gradually displaced the connate water out of the domain. With the displacement of the water and the advance of the dissociation front depicted in Figure 9 at t=30 s, the injected gas quickly broke through the channel, thus dividing the domain into the post-generated preferential flow region and the bubble-trapped region as well. Similar to the low initial water saturation situation, the hydrate dissociation occurring in the bubble-trapped regions was much slower than that in the preferential flow region, developing the same dissociation wormhole. A different observation was that some residual water upstream slowed down the local dissociation rate, which caused partial hydrate near the entrance to be not completely dissolved until t=150 s.

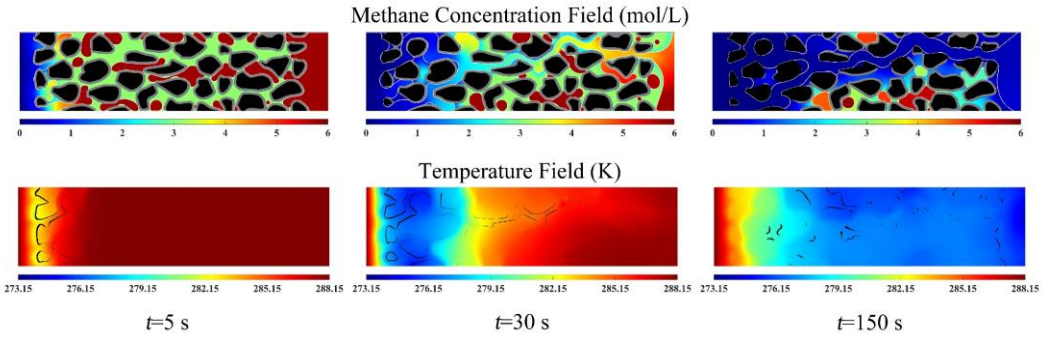

Figure 9 The temporal evolution of the methane concentration (top) and temperature (bottom) during the methane hydrate dissociation process with initial water saturation of $S_w = 0.55$ and the high Pe condition of Pe=0.25.

After understanding the wormholing dissociation characteristic in the multiphase system with the high Pe number, the *C-T* trajectory of two representative locations in the pore space was analyzed with respect to the hydrate dissociation equilibrium curve in Figure 10 to demonstrate the dissociation mechanism at the two distinctive regions.

The methane concentration was computed using the equivalent value of the gas phase as $C_g = C/\left(Hx_w + 1 - x_w\right)$. The two locations were marked as PFR, located in the preferential flow region, and BTR, sitting in the bubble-trapped region, marked in Figure 8(a) at t=5 s. The PFR and BTR were initially prescribed at the same phase equilibrium condition, but they experienced different C-T trajectories into the unstable state. As for the low initial water of $S_w = 0.13$ in Figure 10(a), the methane concentration and temperature at PFR decreased under the phase equilibrium line to trigger hydrate dissociation at the early time. Afterward, the time-dependent temperature and concentration at PFR almost declined parallel to the phase equilibrium curve till t=100 s due to the dissociation endotherm and the sustainable low-methane-concentration gas convection in the preferential flow region. At t=100 s, the methane concentration at PFR reduced close to zero as the injected methane concentration. The approximately stable fugacity gap but the continuous decreasing temperature at PFR suggest that the heat-transfer-limitation was the critical mechanism to restrict the hydrate dissociation in the preferential flow region. By contrast, Figure 10(a) indicates the methane concentration at BTR was almost unchanged before 50 s due to the dramatic mass-transfer-limitation while the temperature significantly decreased by heat conduction. Then, the methane concentration at BTR dropped slowly and reached the equilibrium line after t=400 s, indicating that the methane hydrate was notably delayed at BTR. Accordingly, both the mass-transfer-limitation and heat-transfer-limitation were concluded to significantly inhibit the hydrate dissociation in the bubble-trapped region till 400 s.

Figure 10(b) illustrates the *C-T* trajectories at PFR and BTR with the high initial water saturation. The *C-T* trajectory at PFR shows a similar pattern as the low initial water saturation due to the rapid displacement of the connate water out of the domain by the high-speed gas injection. However, the methane concentration at BTR decreased much slower than the low initial water saturation situation. As observations, the methane concentration at BTR started to drop at t=200 s and did not enter the unstable dissociation state even at 500 s. From the phase distribution in Figure 9, the residual water in the bubble-trapped region for $S_w = 0.55$ was more abundant than $S_w = 0.13$, bringing an intensified mass-transfer-limitation and thus little hydrate dissociation before 500 s. Overall, the different *C-T* trajectories at PFR and BTR further interpreted the formation mechanism of the wormholing dissociation and distinguished the role of heat and mass transport mechanisms to limit the hydrate dissociation at the preferential flow and bubble-trapped regions.

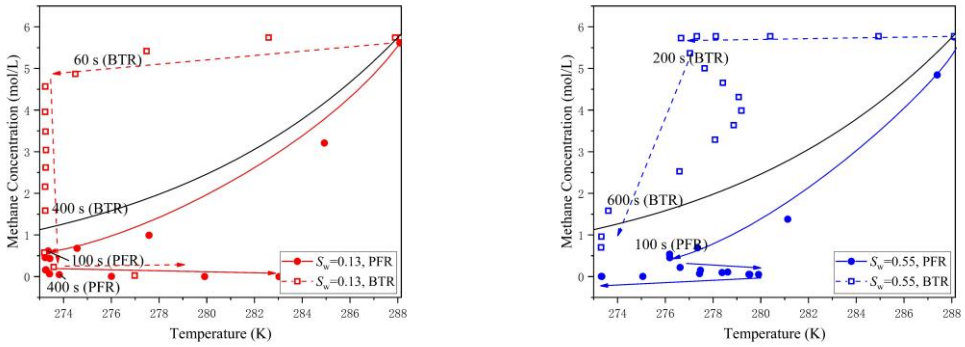

(a) (b)

Figure 10 The *C-T* trajectory of the two representative locations: PFR (the point in the preferential flow region) and BTR (the point in the bubble-trapped region) during the methane hydrate dissociation with (a) $S_w = 0.13$, (b) $S_w = 0.55$, and high Pe

condition (Pe=0.25). The black line is the phase equilibrium line of the methane hydrate, while solid arrowed lines and dashed arrowed lines denote the evolution direction of the methane concentration and temperature over time. Time instants were labeled close to some markers.

Figure 11 compares temporal profiles of methane hydrate saturation among different initial water saturation situations, including the single-phase case, to figure out the effect of water saturation on the concerned hydrate recovery rate in engineering. The hydrate saturation profiles are observed to nonlinearly decrease with time regardless of the single-phase and multiphase problems, which agree with the intensified mass-transfer-limitation or heat-transfer-limitation with the advance of the hydrate dissociation as discussions in Section 3.1 and 3.2.1. However, the counterintuitive finding is the hydrate dissociation rates in the multiphase system are comparative to the single-phase situation at the methane convective transport-limited regime (high Pe condition) without the difference in magnitude. The hydrate dissociation rate with the initial saturation of 0.13 even prevailed over the single-phase situation after 200 s when the dissociation mainly emerged in the bubble-trapped regions.

Temporal evolutions of volume-averaged methane concentration and temperature are displayed in Figure 12(a) and (b) to help analyze the effect of water saturation on the hydrate dissociation rate. The heat-transfer-limitation and mass-transfer-limitation were quantified for the varying water saturation in Figure 13 to further elucidate the competitive mechanisms of these two limitations. During quantification, three

numerical dissociation processes were compared, including: (1) isothermal single-phase dissociation without involving heat transfer and multiphase mass transfer; (2) isothermal multiphase dissociation without considering heat transfer; (3) normal multiphase dissociation. At a fixed time instant, the hydrate recovery rate difference between process (1) and process (2) was used to characterize the mass-transfer-limitation, while the hydrate recovery rate difference between process (2) and process (3) was measured to represent the heat-transfer-limitation.

Figure 12(a) shows that the decreasing volume-averaged methane concentration profile in the single-phase situation kept ahead of other multiphase scenarios due to the mass-transfer-limitation. Meanwhile, the volume-averaged methane concentration profiles in the multiphase system represent two stages, comprising of the linear interval (t<50 s) where hydrate dissociation occurred in the preferential flow region and the exponential interval (t>50 s) where hydrate dissociation primarily took place in the bubble-trapped region. At the first stage, the hydrate dissociation dynamics in the preferential flow region was similar to the single-phase situation but presented some mass-transfer-limitation by the thin covered water layer, resulting in slightly lower hydrate dissociation rates. However, during the second stage, the increasing water saturation slowed down the reduction of the methane concentration due to more significant mass-transfer-limitation in the bubble-trapped region, as showed in Figure 13. As to the heat transfer limitation, Figure 12(b) shows that the single-phase situation quickly dropped into the freezing condition at 100 s and maintained the imperceptible hydrate dissociation for a long time due to the heat-transfer-limitation. Oppositely, the

volume-averaged temperature decreased less slowly for the higher initial water saturation as a result of the increasing heat capacity of the water phase. Moreover, the volume-averaged temperature in some multiphase cases terminated declining at the second stage but rose away from the freezing condition, which agrees with the temperature rising for both high and low water saturation in Figure 10. The extraordinary temperature rising can be interpreted by that the hydrate was gradually exhausted in the faster region, and the weak dissociation endotherm in the neighboring bubble-trapped region could not outweigh the positive impact of the injected high-temperature gas (288.15 K, initial temperature). Furthermore, the volume-averaged temperature rebounded earlier and more remarkably with the increasing water saturation due to the enlarged bubble-trapped region. Therefore, the heat-transfer-limitation decreased with the increasing water saturation at the second stage. Figure 13 shows that the weakened heat-transfer-limitation could balance the intensified mass-transfer-limitation with the growing water saturation, leading to the comparative hydrate dissociation rate. Despite the single-phase situation ($S_w = 0$) experienced no mass-transfer-limitation, the intensified heat-transfer-limitation was equivalent to the sum of two limitations in the multiphase cases. Therefore, the competitive mechanism of the heat-transfer-limitation and the mass-transfer-limitation resulted in the comparative hydrate dissociation rate regardless of the water saturation for the high Pe conditions. Despite the comparative dissociation rate, the hydrate dissociation pattern varied from the conical dissociation in the single phase to the wormholing dissociation in the multiphase, which can influence the concerning evolution of the sediment

permeability in engineering and will be discussed in Section 3.4.

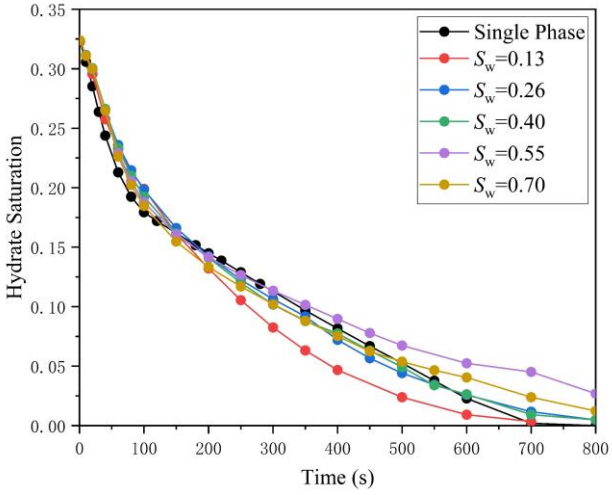

Figure 11 Comparisons of temporal variation of methane hydrate saturation among different initial water saturation situations when Pe=0.25.

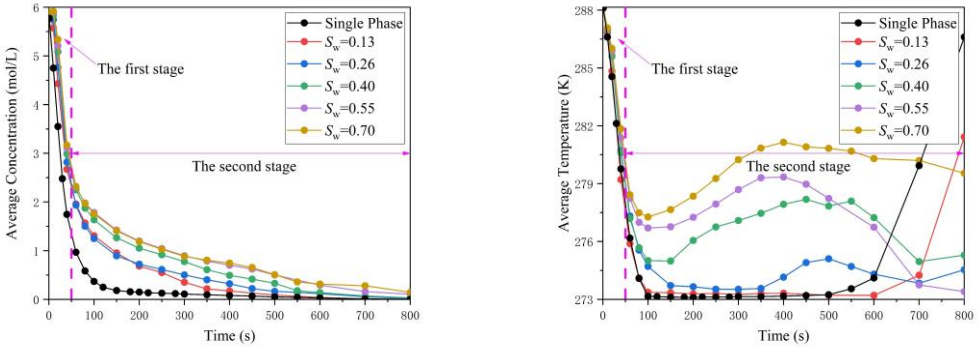

(a) (b)

Figure 12 Comparisons of the temporal evolution of average (a) methane concentration and (b) temperature over the computational domain among different initial water saturation situations when Pe=0.25.

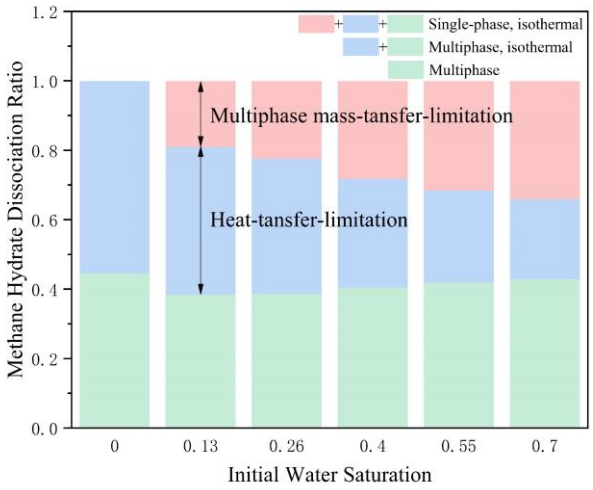

Figure 13 Quantification of the heat-transfer-limitation and mass-transfer-limitation with different initial water saturation at t=100 s for Pe=0.25. The pink and blue stacked bar heights represent the relative magnitude of the mass-transfer-limitation and heat-transfer-limitation, respectively. The dissociation ratio was computed as $\eta = 1 - S_{\mathrm{hyd}}(t) / S_{\mathrm{hyd0}}$.

3.2.2 Low Pe condition

The multiphase hydrate dissociation dynamics were investigated with the low gas injection rate (Pe=0.0025), where the diffusion dominated the methane transport. Figure 14 shows the facial dissociation dynamics with the low initial water saturation of $S_{\mathrm{w}} = 0.13$. At the beginning (t=10 s), the hydrate dissociation proceeded into the domain through the interconnected gas pathways, similar to the single-phase situation at the diffusion-limited regime. With the development of the hydrate dissociation, the produced water from the hydrate dissociation was absorbed on the hydrate surface or trapped in the pore throat due to the insufficient displacement force of the low gas

injection rate, as indicated in Figure 15. The water barrier then facilitated the growth of the bubble-trapped region, leading to the significant mass-transfer-limitation at the dissociation front in Figure 14 at t=100 s. Compared to the single-phase diffusion, the slow interphase methane diffusion strongly inhibited the hydrate dissociation. Meanwhile, the advancement of the dissociation front was observed to accomplish with the propagation of the high methane concentration within the bubble-trapped region, as shown in Figure 14 at t=500 s, displaying the facial dissociation pattern. The multiphase hydrate dissociation at the low initial water saturation and low Pe condition shared the same facial dissociation pattern with the single-phase dissociation; however, the underlying dissociation limitation mechanism varied from these two scenarios. Qualitatively comparing the temperature evolution at Figure 6 (single-phase dissociation) and Figure 14 (multiphase dissociation), the decreasing temperature of the multiphase dissociation was found to evolve less slowly than the single-phase dissociation, indicating that heat-transfer-limitation competed for the mass-transfer-limitation in the multiphase system. More quantification of these two limitation roles will be discussed after introducing the multiphase dissociation with the high water saturation.

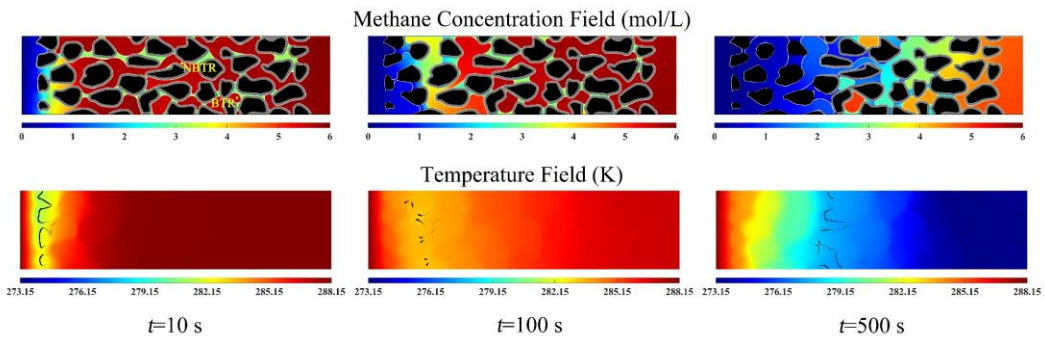

Figure 14 The temporal evolution of the methane concentration (top) and temperature (bottom) during the methane hydrate dissociation process with the low initial water saturation of $S_w = 0.13$ under the low Pe condition of Pe=0.0025.

(a)

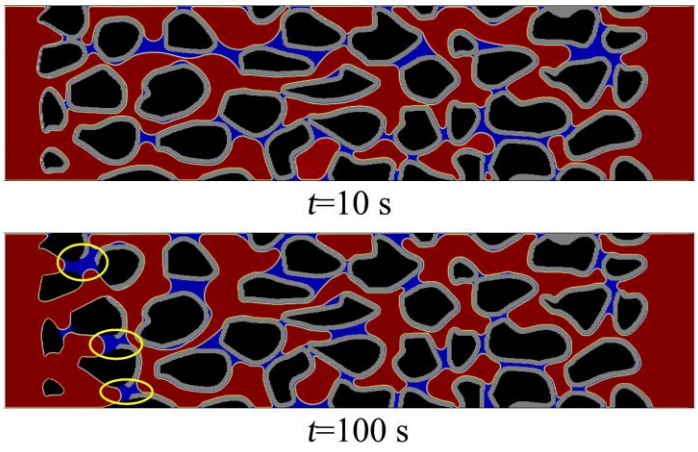

(b)

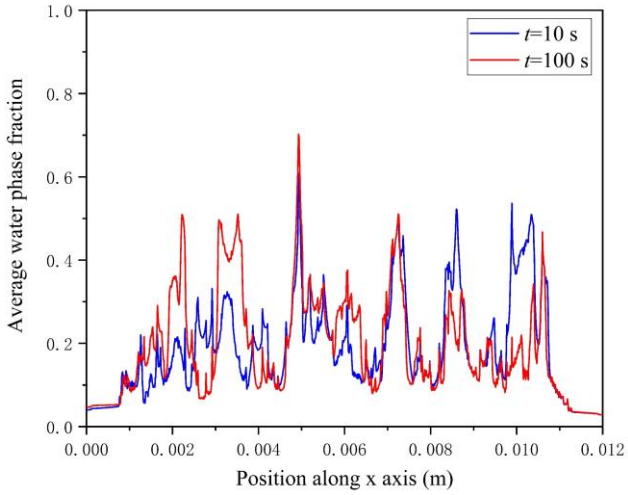

Figure 15 (a) Comparison of phase distribution at t=10 s and t=100 s with $S_w = 0.13$. The red color denotes the gas phase, and the blue color represents the water phase. (b) Average water fraction over each cross-section along the horizontal direction at t=10 s and t=100 s. At x=0.002 m, the water fraction within the hydrate dissociation region at t=100 s increased significantly compared to that at t=10 s. The generated water barrier is circled with yellow in the phase distribution contour of t=100 s,

indicating that the generated water blocked the gas pathway.

For the multiphase dissociation at the high connate water saturation of $S_w = 0.55$ and low Pe number of Pe=0.0025 in Figure 16, the same facial dissociation pattern was still observed but with the varying dissociation dynamics. Figure 16 shows sustainable pore space was filled with the connate water without the pre-existing continuous gas pathway, indicating that the original bubble-trapped region almost occupied the domain. The detectable hydrate dissociation was constrained within the water displacement front and initiated near the gas-water interface, driven by the methane interfacial diffusion transport. Oppositely, the methane preserved a high concentration at the downstream bubble-trapped region far from the displacement front, leading to the stable phase equilibrium and thus unnoticeable hydrate dissociation. Accordingly, the hydrate dissociation advanced with the creeping water displacement by the low-speed injected gas. Moreover, as observations of the retarded temperature decrease in Figure 16, the mass-transfer-limitation is implied to become the most vital mechanism to suppress the dissociation with the high water saturation and low Pe condition.

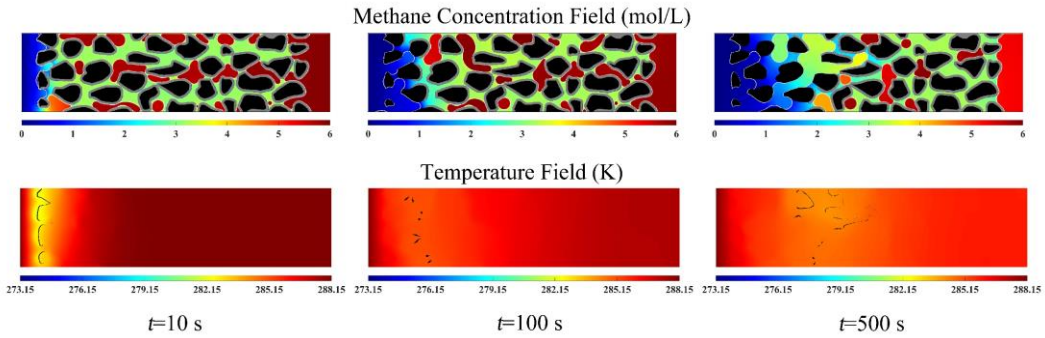

Figure 16 The temporal evolution of the methane concentration (top) and temperature (bottom) during the methane hydrate dissociation process with initial water saturation

$S_w = 0.55$ under the low Pe condition of Pe=0.0025.

To further distinguish the underlying dissociation mechanism among the low/high water saturation and the low/high Pe number, the *C*-*T* trajectories of two representative locations, NBTR (Non-bubble-trapped region) and BTR, are plotted in Figure 17 and compared to Figure 10. The NBTR point presents the location where the fluid can move forward with gas injection instead of being trapped in the sediment as marked in Figure 14 at *t*=10 s, which is in the same position as PFR in Figure 8(a). Figure 17(a) shows that the methane at NBTR maintained the initial high concentration above the phase equilibrium line till *t* =100 s, different from the PFR in Figure 10(a), where the methane concentration quickly dropped below the phase equilibrium line. After *t* =100 s, the methane concentration at NBTR decreased slowly, with the duration reaching the phase equilibrium line (*t* =800 s) being around one order of magnitude longer than the PFR in Figure 10(a). The slowing down methane concentration evolution at NBTR came from the disappearance of the preferential flow region with the low Pe number, subsequently controlled by the weak interphase diffusion as BTR. The BTR in Figure 17(a) presents a similar *C*-*T* trajectory to the BTR in Figure 10(a). However, the BTR in Figure 17(a) did not enter the unstable dissociation zone even at *t*=800 s, indicating no hydrate could be dissolved at the BTR before 800 s due to the enhanced mass-transfer-limitation with the low Pe number. In general, the delayed *C*-*T* trajectories in Figure 17(a) suggest the mass-transfer-limitation is intensified with the decreasing Pe number.

As to the high initial water saturation of $S_w = 0.55$, Figure 17(b) indicates the

methane at the NBFR and BTR started to decrease at t=400 s and t=600 s, respectively, much postponed compared to the NBTR and BTR with the lower water saturation in Figure 17(a). Oppositely, the temperature at the NBTR and BTR in Figure 17(b) merely dropped by 5 K at t=800 s, much lower than the NBTR and BTR in Figure 17(a). The different *C-T* trajectories between Figure 17(a) and 17(b) imply the competitive relationship of the heat-transfer-limitation and the mass-transfer-limitation significantly varied from the water saturation with the low Pe number. With the increasing water saturation at the low Pe, the dissociation limitation gradually changed from the contribution of both heat-transfer-limitation and mass-transfer-limitation to the dominance by the mass-transfer-limitation.

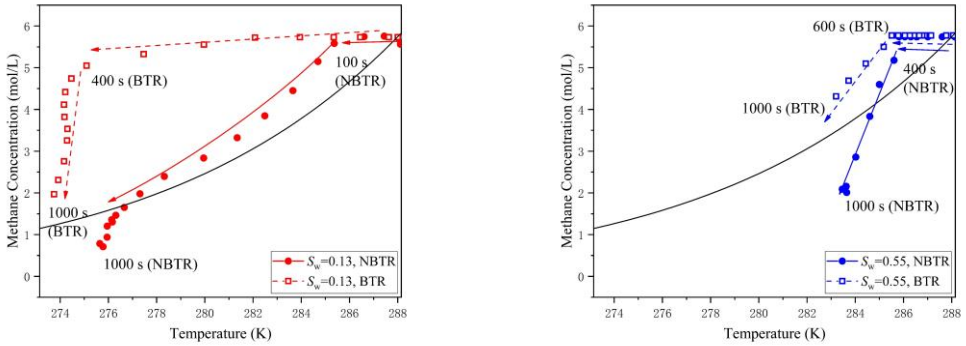

(a) (b)

Figure 17 The *C-T* trajectory of the two representative locations NBTR (in outside the bubble-trapped region) and BTR (in the bubble-trapped region) during the methane hydrate dissociation with (a) $S_w = 0.13$, (b) $S_w = 0.55$ under low Pe condition (Pe=0.0025).

To elucidate the competitive mechanism of the heat-transfer-limitation and mass-transfer limitation during the multiphase hydrate dissociation with the low Pe condition,

the effect of water saturation on temporal profiles of hydrate saturation was compared in Figure 18. Meanwhile, temporal evolutions of the averaged methane concentration and temperature are depicted in Figure 19(a) and (b) with the quantitative heat-transfer-limitation and mass-transfer-limitation measured in Figure 20. Figure 18 shows that the dissociation rates of the multiphase hydrate dissociation with the low Pe condition are fairly linear and much lower than that of the single-phase dissociation, which agrees with the observation of the intensified mass-transfer-limitation according to the dissociation dynamics above. Moreover, Figure 18 indicates that the effect of water saturation on the dissociation rate is negligible with the nearly overlapped temporal profiles of hydrate saturation. The underlying reason can be first interpreted by the observation in Figures 19(a) and (b). Both the average methane concentration and temperature of the low saturation cases dropped more quickly in the low water saturation cases, which could provide positive and negative feedback to the hydrate dissociation rate, respectively. From the quantitative analyses, the dissociation limitation measurement for the low Pe condition in Figure 20 clearly illustrates that the sum of the heat-transfer-limitation and mass-transfer-limitation for all the multiphase dissociation are almost equal but more significant than the heat-transfer-limitation of the single-phase dissociation. Specifically, the heat-transfer-limitation and mass-transfer-limitation are comparable in magnitude for the low water saturation of 0.13. In contrast, the mass-transfer-limitation gradually dominated the hydrate dissociation dynamics with the increasing water saturation, particularly when the water saturation exceeded 0.55. Additionally, the comparison of Figures 13 and 20 also reveals that the

increasing Pe number weakens the mass-transfer-limitation but improves the heat-transfer-limitation, which is in accordance with the analyses in Section 3.2.1. Consequently, other than the low Pe condition, both the mass-transfer-limitation and heat-transfer-limitation cannot be negligible regardless of the water saturation for the high Pe condition.

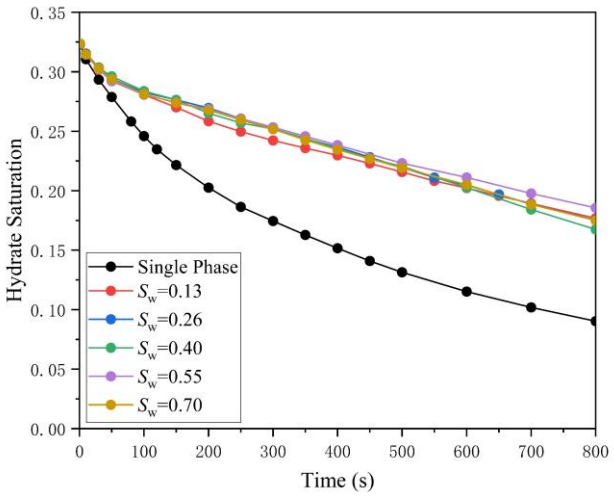

Figure 18 Comparisons of temporal variation of methane hydrate saturation among different initial water saturation situations when Pe=0.25.

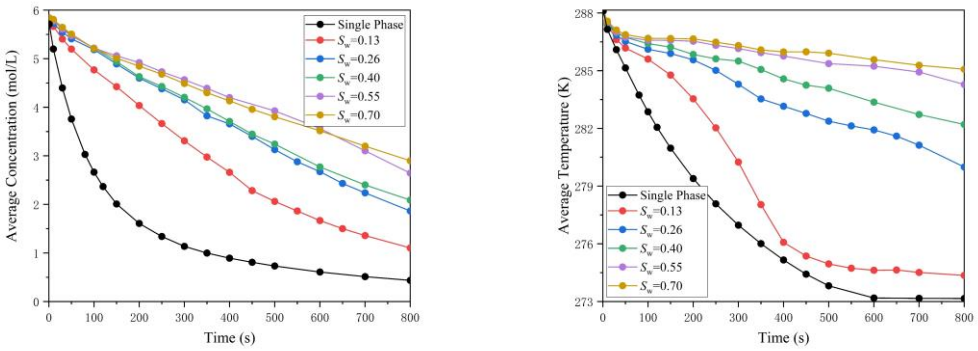

(a) (b)

Figure 19 Comparisons of the temporal evolution of average (a) methane concentration and (b) temperature over the computational domain among different

initial water saturation situations when Pe=0.0025.

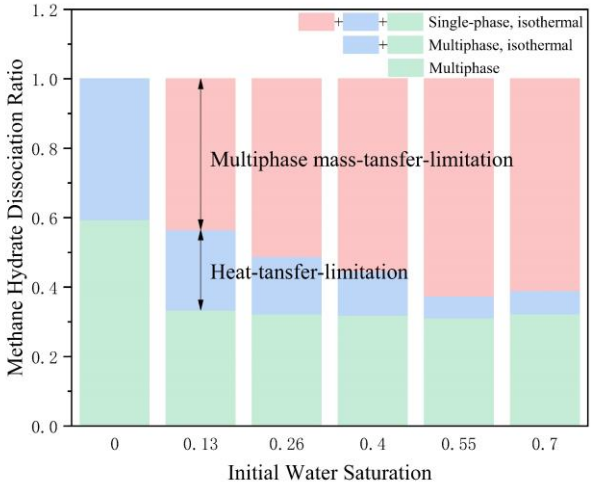

Figure 20 Quantification of the heat-transfer-limitation and mass-transfer-limitation with different initial water saturation at *t*=500 s for Pe=0.0025.

3.3 Regime diagram of methane hydrate dissociation

Figure 21 summarizes the initial water saturation-Pe diagram of the methane hydrate dissociation dynamics, comprising five different dissociation regimes mapped by the dissociation pattern, the dominant mass transport mechanism, and the dominant dissociation limitation mechanism. The regime boundary of $Pe \sim O(10^{-2})$ splits the diagram into the top and bottom subdivisions. When $Pe > O(10^{-2})$, hydrate dissociation patterns exhibit the conical dissociation for the single phase and the wormholing dissociation for the multiphase. In the conical dissociation regime for the single phase, the mass transport is controlled by convection, while the dissociation rate is limited by heat transfer. In the wormholing dissociation regime for the multiphase, the mass transfer is controlled by convection in the preferential flow region but interphase diffusion-limited in the bubble-trapped region. The dissociation efficiency is

determined by the interplayed mass-transfer-limitation and heat-transfer-limitation. When $\mathrm{Pe} < \mathrm{O}(10^{-2})$, the mass transport is controlled by diffusion mechanism (interphase diffusion for the multiphase), and the dissociation presents the facial dissociation dynamics regardless of initial water saturation. According to the various dissociation limitations, however, two different regimes are further separated by the water saturation of about 0.5. For the water saturation less than 0.5, both heat-transfer-limitation and mass-transfer-limitation determined the dissociation rate. In contrast, for the water saturation higher than 0.5, the mass-transfer-limitation was dominant to influence the dissociation process. To the best of our knowledge, the methane dissociation regime diagram is firstly introduced by the present study to better visualize the effect of the Pe and initial water saturation on the dissociation dynamics and inherent mechanisms. Owing to the phase diagram, the pore-scale numerical simulation enlightens the REV-scale simulation model to take non-negligible physics into account for accurate hydrate recovery forecast at the various dissociation conditions. Some discussions on the modeling of heat transfer and multiphase mass transfer in the REV-scaled simulation have been reported in our previous studies [24, 49]. What should be mentioned here is the regime boundaries of the Pe number and initial water saturation may vary from the sediment structure, the grain wettability, and the hydrate pore habit, which still need more investigation in future work.

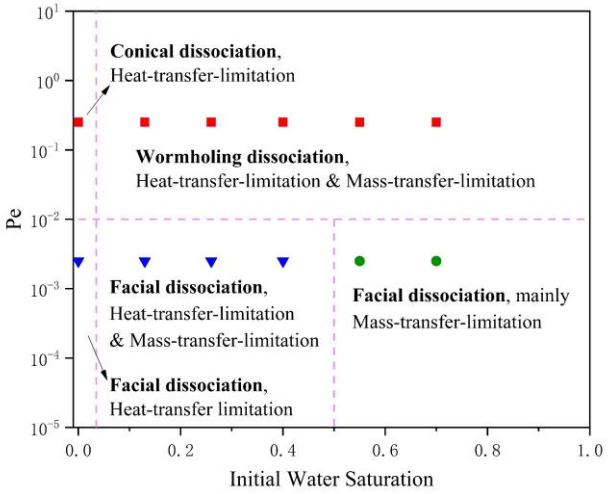

Figure 21 Regime diagram of the methane hydrate dissociation with different Pe and initial water saturation. The texts label the dissociation pattern and the dominant dissociation limitation mechanism in order. The marker denotes the performed simulation in the present study.

3.4 Volume-averaged properties for REV-scale modeling

After analyzing the methane hydrate dissociation regimes, the volume-averaged transport and geometric properties were investigated to benefit the REV-scale modeling, including the evolution of the absolute permeability and hydrate surface area with hydrate saturation. Figure 22 shows the relationship of the normalized permeability K (the absolute permeability divided by the sediment permeability with no hydrate) and the hydrate saturation varied with the specific dissociation pattern, comprising the wormholing dissociation, conical dissociation, and facial dissociation. For the wormholing dissociation pattern, the permeability evolution presents two stages in line with the previous observation with wormholing dissolution phenomena [59]. The nonlinear and significant variation when $S_{\mathrm{hyd}} > 0.2$ comes from the fact that the

injected fluid can migrate preferentially through the new or enwidened pathway created by the dissociation wormhole, where the wormhole aperture determines the flow resistance. With the dissociation developing into the bubble-trapped region, the uniform dissociation could not make other large channels but slowly enlarge the pore throat, leading to linear permeability increase with a declined slope. Compared with the wormholing dissociation pattern, the permeability increased less steep within the interval of $S_{hyd} > 0.2$ for the conical dissociation due to the narrowed preferential pathway, and least steep for the facial dissociation due to the disappearance of the preferential pathway. Additionally, the two-stage feature of the permeability-hydrate saturation relationship vanished instead of a nonlinear variation for the conical and facial dissociation, which is also attributed to the varying dissociation dynamics.

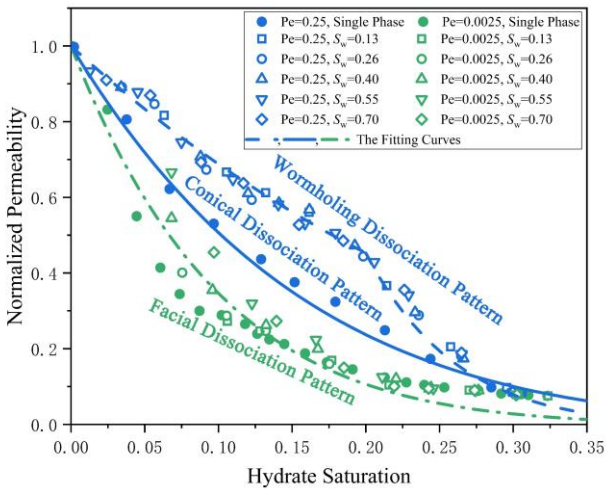

Figure 22 Permeability-hydrate saturation for three dissociation patterns. The markers denote the numerical results, while the lines depict the fitting curves.

In reality, considerable empirical relations have been proposed to quantify the permeability related to hydrate saturation. However, the previous studies [46, 47]

usually consider the permeability-hydrate saturation relation during the hydrate nucleation and formation process with little attention to the multiphase hydrate dissociation. To improve the prediction of the permeability evolution during different dissociation dynamics, the empirical relation between the normalized permeability K and hydrate saturation S_{hyd} permeability was revisited using the Tokyo model [60] as

$$K = \left(1 - S_{\mathrm{hyd}}\right)^{N} \tag{23}$$

where N is the fitting microstructural parameter. Additionally, considering the two-stage permeability evolution for the wormhole dissociation, the permeability was piecewise fitted as

$$K = \begin{cases} a\left(1 - S_{\mathrm{hyd}}\right)^{N_1}, & S_{\mathrm{hyd}} > 0.2 \\ \left(1 - S_{\mathrm{hyd}}\right)^{N_2}, & S_{\mathrm{hyd}} \le 0.2 \end{cases} \tag{24}$$

As shown in Figure 22, an exponent N=6.45 fits well the conical dissociation pattern with the fitting error of about 10%, while N=9.00 fits the facial dissociation pattern acceptably regardless of the single-phase and multiphase dissociation and with the fitting error ranging from 25% to 30%. For the wormholing dissociation pattern, the piecewise fitting coefficient and exponents are $N_1 = 13.12$, $N_2 = 3.55$, $a = 8.46$, respectively, with the fitting error of nearly 10%. By comparison to Chen et al.'s [47] work on the hydrate formation, their fitting result of N=6.20 corresponded to our results for the conical dissociation pattern. For the facial and wormholing dissociation pattern, the hydrate distribution tended more heterogeneous over the sediment as the dissociation proceeded, resulting in the increasing N factors. Therefore, the necessity is emphasized to model the permeability evolution precisely by considering the

dissociation pattern in the REV-scale simulation.

The variation of the total hydrate surface area with the residual hydrate saturation is illustrated in Figure 23, indicating that the hydrate surface area profile slightly varied from the Pe number but was little impacted by the water saturation. Therefore, the effect of the dissociation pattern on the hydrate surface area is less important than the permeability, which is consistent with the previous work [59]. The fitting model for the hydrate surface area can be written as [23]

$$A_s = b \cdot S_{hyd}^m \tag{25}$$

The fitting parameter m for the different simulation cases varied from $m = 0.8$ to $m = 0.9$ with an average b value as $b = 3.28 \times 10^{-6}$ m^2. The average m=0.85 is recommended to predict the hydrate surface area in the REV-scale modeling with less than 20% fitting error, as illustrated in Figure 23.

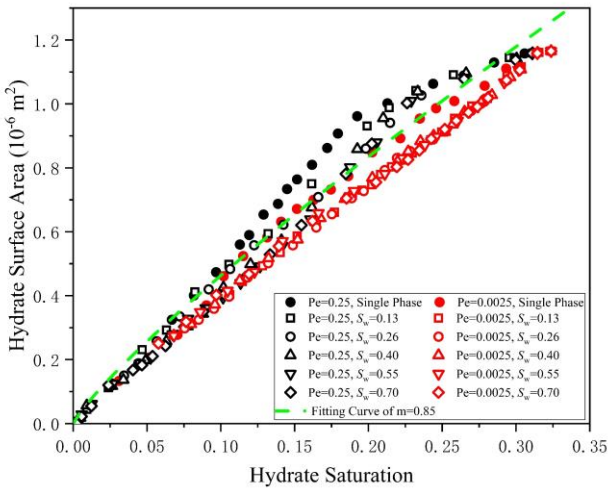

Figure 23 Hydrate Surface Area - Hydrate saturation relationship for different initial water saturation and Pe conditions.

4. Conclusions

A pore-scale numerical model based on the lattice Boltzmann method was proposed to investigate the multiphase methane hydrate dissociation in the sediment, including multiphase flow, heat and mass transfer, dissociation reaction, and hydrate structure evolution. Base cases, single-phase hydrate dissociation, were firstly simulated to demonstrate the conical dissociation pattern at the convection transport-limited regime ($Pe > O(10^{-2})$) and the facial dissociation pattern at the diffusion transport-limited regime ($Pe < O(10^{-2})$). Meanwhile, two characteristic Pe numbers, 0.0025 and 0.25, were identified for the multiphase dissociation in the specified sediment porous medium. Particular interest is then paid to explore the effect of the water saturation and the Pe number on the multiphase dissociation dynamics and inherent mechanisms resulting from the interplay between the mass-transfer-limitation and heat-transfer-limitation.

For the high Pe condition (Pe=0.25), the dissociation wormhole was observed with the preferential flow region and the bubble-trapped region regardless of the connate water saturation, leading to the heterogeneous dissociation in space and the nonlinear dissociation rate over time. The analyses of *C*-*T* trajectories in the hydrate equilibrium phase diagram for the two distinctive dissociation regions indicate that the heat-transfer-limitation dominated the preferential flow region similar to the single-phase situation, while the mass-transfer-limitation developed within the bubble-trapped region to delay the hydrate dissociation significantly. For the low Pe condition (Pe=0.0025), the facial dissociation was revealed where the dissociation front advanced

with the slow interphase methane diffusion and the gas-water displacement. Compared to the high Pe condition, the multiphase hydrate dissociation presented a linear but lower dissociation rate. Comparisons of the *C*-*T* trajectories and the quantification of the heat-transfer-limitation and mass-transfer-limitation demonstrate that the decreasing Pe number gradually improved the mass-transfer-limitation but weakened the heat-transfer-limitation. The heat-transfer-limitation cannot be negligible, except the high connate water saturation at the low Pe condition, which was prominently limited by the methane interfacial mass transfer. Moreover, the competitive limitation mechanisms led to the effect of water saturation on the hydrate dissociation rate being negligible for the low Pe conditions.

Five hydrate dissociation regimes were mapped on the connate water saturation-Pe diagram to elucidate the various dissociation dynamics with the dominant methane transport mechanism and primary dissociation limitation mechanism. The volume-averaged transport and geometric properties, the permeability and the specific surface area, were corrected with the residual hydrate saturation to yield the empirical relations suitable for three typical dissociation patterns instead of the previous models for the hydrate formation. The mapped dissociation regime and the developed empirical correlations can enable more accurate REV-scaled modeling of different dissociation dynamics by taking the addressed essential physics and precise volume-averaged properties into account.

In the future, more details on REV-scaled modeling will be investigated. Different operation and formation conditions, such as formation/well pressure and temperature,

will be studied with various hydrate pore-habits, including the pore-filling and grain-coating pattern, to understand more dissociation mechanisms during the hydrate depressurization recovery.

Acknowledgment

This work was financially supported by the National Natural Science Foundation of China (No. 51876100), Open-Project Program of the State Key Laboratory of Chemical Engineering (grant number: SKL-ChE-21A04), and the Science Fund for Creative Research Group (No. 51621062).

Appendix

To verify the reliability of the numerical models in the present work, the experimental process of hydrate dissociation in Figure A1 was simulated. The water layer thickness in the micro-CT image became uniform as the dissociation progressed, suggesting the mass-transfer-limitation within the water layer influences the dissociation rate [33]. More details about the discussion of mass-transfer-limitation influence on the experiment process, and the numerical settings such as the governing equations and boundary conditions can be found in our previous work [24].

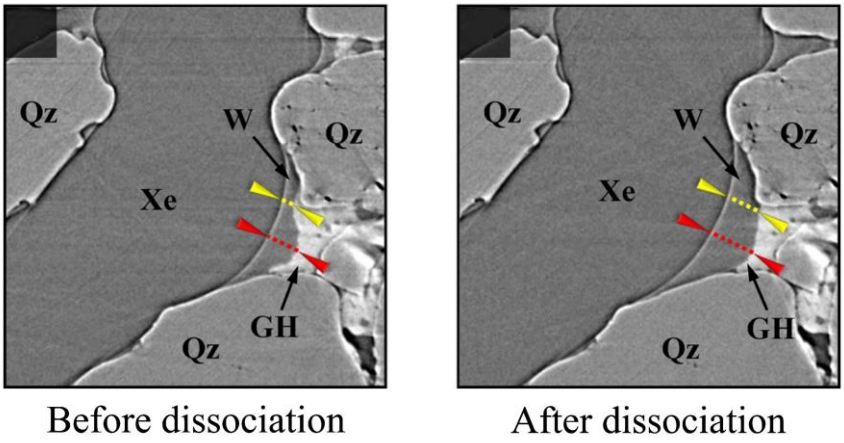

Figure A1 Micro-CT image of hyrate dissociation in Yang et al.'s work [33]. 'W' denotes the water layer and 'GH' denotes the hydrate structure.

In the simulation, the initial temperature was 280.13 K, corresponding to the equilibrium concentration of $C_{\mathrm{eq,\,g}} = 2.55$ mol/L . The gas-water distribution and hydrate structure were set the same as the experimental image before dissociation in Figure A1 (left). At the beginning of the simulation, the methane concentration in the gas phase was set as 0.4 mol/L, lower than the equilibrium value. As a result, the hydrate equilibrium was broken, and the dissociation started. The simulation results of the hydrate dissociation process are shown in Figure A2. Due to the low methane diffusivity in the water phase, the methane concentration near the hydrate surface maintained high values. As a result, the fugacity difference at the water-hydrate interface decreased, slowing down the hydrate dissociation rate, regarded as mass-transfer-limitation. The hydrate covered by the thicker water layer dissolved more slowly due to the stronger local mass-transfer-limitation, resulting in the uniform water layer thickness after dissociation. This mechanism is consistent with the phenomenon observed in the experiment. Figure A3 compared the final residual hydrate structure of the numerical

and experimental results after the hydrate was dissolved 12%. The satisfactory agreement indicates the numerical models of the present work can simulate the methane hydrate dissociation process accurately.

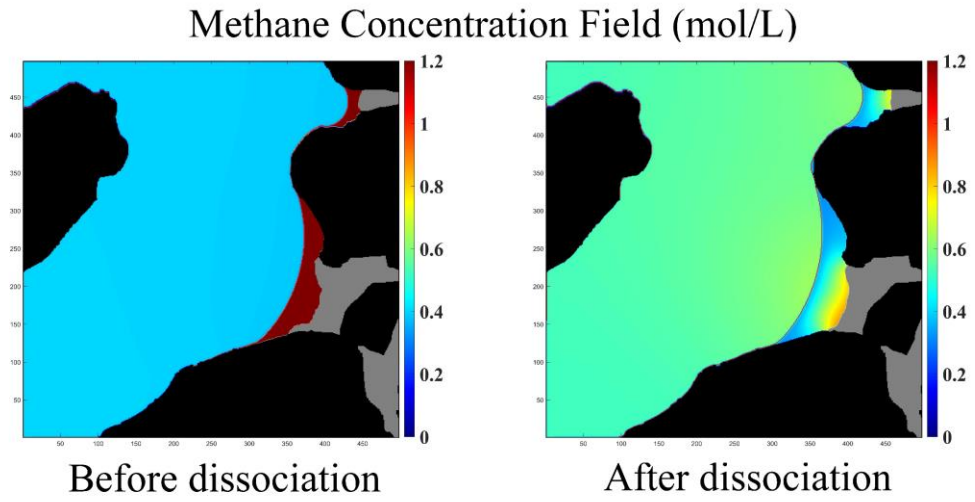

Figure A2 Numerical results of concentration evolution in the simulation of experimental process. The gas-water interface is denoted be red line in the concentration contour map.

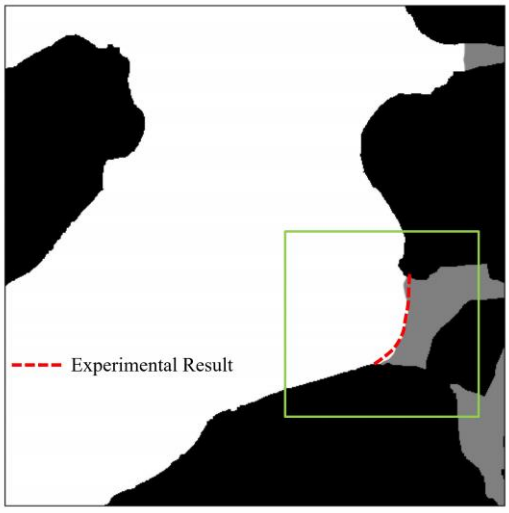

Figure A3 Comparison of the residual hydrate structure of numerical and experimental results. The experimental results are depicted in the red dotted line.

References

[1] J.Y. Lee, B.J. Ryu, T.S. Yun, J. Lee, G.-C. Cho, Review on the gas hydrate development and production as a new energy resource, KSCE Journal of Civil Engineering 15 (2011) 689-696.

[2] C.A.K. E. Dendy Sloan Jr., Clathrate Hydrates of Natural Gases, CRC Press2007.

[3] J. Wei, Y. Fang, H. Lu, H. Lu, J. Lu, J. Liang, S. Yang, Distribution and characteristics of natural gas hydrates in the Shenhu Sea Area, South China Sea, Marine and Petroleum Geology 98 (2018) 622-628.

[4] J. Kan, Y. Sun, B. Dong, Q. Yuan, B. Liu, C. Sun, G. Chen, Numerical simulation of gas production from permafrost hydrate deposits enhanced with CO2/N2 injection, Energy 221 (2021) 119919.

[5] S.Y. Lee, G.D. Holder, Methane hydrates potential as a future energy source, Fuel Processing Technology 71 (2001) 181-186.

[6] Y. Song, L. Yang, J. Zhao, W. Liu, M. Yang, Y. Li, Y. Liu, Q. Li, The status of natural gas hydrate research in China: A review, Renewable and Sustainable Energy Reviews 31 (2014) 778-791.

[7] Z.R. Chong, S.H.B. Yang, P. Babu, P. Linga, X.S. Li, Review of natural gas hydrates as an energy resource: Prospects and challenges, Applied Energy 162 (2016) 1633-1652.

[8] L. Chen, Y. Feng, T. Kogawa, J. Okajima, A. Komiya, S. Maruyama, Construction and simulation of reservoir scale layered model for production and utilization of methane hydrate: The case of Nankai Trough Japan, Energy 143 (2018) 128-140.

[9] B.J. Anderson, M. Kurihara, M.D. White, G.J. Moridis, S.J. Wilson, M. Pooladi-

Darvish, M. Gaddipati, Y. Masuda, T.S. Collett, R.B. Hunter, H. Narita, K. Rose, R. Boswell, Regional long-term production modeling from a single well test, Mount Elbert Gas Hydrate Stratigraphic Test Well, Alaska North Slope, Marine and Petroleum Geology 28 (2011) 493-501.

[10] W.X. Pang, W.Y. Xu, C.Y. Sun, C.L. Zhang, G.J. Chen, Methane hydrate dissociation experiment in a middle-sized quiescent reactor using thermal method, Fuel 88 (2009) 497-503.

[11] C. Ji, G. Ahmadi, D.H. Smith, Natural gas production from hydrate decomposition by depressurization, Chemical Engineering Science 56 (2001) 5801-5814.

[12] Q. Yuan, C. Sun, X. Yang, P. Ma, Z. Ma, Q. Li, G. Chen, Gas Production from Methane-Hydrate-Bearing Sands by Ethylene Glycol Injection Using a Three-Dimensional Reactor, Energy & Fuels 25 (2011) 3108-3115.

[13] Z. Yin, Z.R. Chong, H.K. Tan, P. Linga, Review of gas hydrate dissociation kinetic models for energy recovery, Journal of Natural Gas Science and Engineering 35 (2016) 1362-1387.

[14] X. Wang, B. Dong, F. Wang, W. Li, Y. Song, Pore-scale investigations on the effects of ice formation/melting on methane hydrate dissociation using depressurization, International Journal of Heat and Mass Transfer 131 (2019) 737-749.

[15] D. Han, Z. Wang, Y. Song, J. Zhao, D. Wang, Numerical analysis of depressurization production of natural gas hydrate from different lithology oceanic reservoirs with isotropic and anisotropic permeability, Journal of Natural Gas Science and Engineering 46 (2017) 575-591.

[16] E. Piñero, C. Hensen, M. Haeckel, W. Rottke, T. Fuchs, K. Wallmann, 3-D numerical modelling of methane hydrate accumulations using PetroMod, Marine and Petroleum Geology 71 (2016) 288-295.

[17] L. Yu, Y. Xu, Z. Gong, F. Huang, L. Zhang, S. Ren, Experimental study and numerical modeling of methane hydrate dissociation and gas invasion during drilling through hydrate bearing formations, Journal of Petroleum Science and Engineering 168 (2018) 507-520.

[18] L. Zhang, L. Yang, J. Wang, J. Zhao, H. Dong, M. Yang, Y. Liu, Y. Song, Enhanced CH 4 recovery and CO 2 storage via thermal stimulation in the CH 4 /CO 2 replacement of methane hydrate, Chemical Engineering Journal 308 (2017) 40-49.

[19] S. Li, G. Zhang, Z. Dai, S. Jiang, Y. Sun, Concurrent decomposition and replacement of marine gas hydrate with the injection of CO2-N2, Chemical Engineering Journal 420 (2021) 129936.

[20] L. Sun, T. Wang, B. Dong, M. Li, L. Yang, H. Dong, L. Zhang, J. Zhao, Y. Song, Pressure oscillation controlled CH4/CO2 replacement in methane hydrates: CH4 recovery, CO2 storage, and their characteristics, Chemical Engineering Journal (2021) 129709.

[21] J. Zhao, D. Liu, M. Yang, Y. Song, Analysis of heat transfer effects on gas production from methane hydrate by depressurization, International Journal of Heat and Mass Transfer 77 (2014) 529-541.

[22] B. Wang, Z. Fan, J. Zhao, X. Lv, W. Pang, Q. Li, Influence of intrinsic permeability of reservoir rocks on gas recovery from hydrate deposits via a combined

depressurization and thermal stimulation approach, Applied Energy 229 (2018) 858-871.

[23] Z. Yin, G. Moridis, Z.R. Chong, H.K. Tan, P. Linga, Numerical analysis of experimental studies of methane hydrate dissociation induced by depressurization in a sandy porous medium, Applied Energy 230 (2018) 444-459.

[24] J. Yang, X. Dai, Q. Xu, Z. Liu, C. Zan, W. Long, L. Shi, Pore-scale study of multicomponent multiphase heat and mass transfer mechanism during methane hydrate dissociation process, Chemical Engineering Journal 423 (2021) 130206.

[25] B. Tohidi, R. Anderson, M.B. Clennell, R.W. Burgass, A.B. Biderkab, Visual observation of gas-hydrate formation and dissociation in synthetic porous media by means of glass micromodels, Geology 29 (2001) 867-870.

[26] M. Muraoka, Y. Yamamoto, N. Tenma, Simultaneous measurement of water permeability and methane hydrate pore habit using a two-dimensional glass micromodel, Journal of Natural Gas Science and Engineering 77 (2020) 103279.

[27] Y. Chen, B. Sun, L. Chen, X. Wang, X. Zhao, Y. Gao, Simulation and Observation of Hydrate Phase Transition in Porous Medium via Microfluidic Application, Industrial & Engineering Chemistry Research 58 (2019) 5071-5079.

[28] S. Almenningen, E. Iden, M.A. Fernø, G. Ersland, Salinity Effects on Pore-Scale Methane Gas Hydrate Dissociation, Journal of Geophysical Research: Solid Earth 123 (2018) 5599-5608.

[29] S. Wang, Z. Cheng, Q. Liu, P. Lv, J. Lv, L. Jiang, Y. Song, Microscope insights into gas hydrate formation and dissociation in sediments by using microfluidics,

Chemical Engineering Journal 425 (2021) 130633.

[30] Z. Zhao, X.P. Zhou, Pore-scale effect on the hydrate variation and flow behaviors in microstructures using X-ray CT imaging, Journal of Hydrology 584 (2020) 124678.

[31] J. Zhao, L. Yang, Y. Liu, Y. Song, Microstructural characteristics of natural gas hydrates hosted in various sand sediments, Phys Chem Chem Phys 17 (2015) 22632-22641.

[32] L. Lei, Y. Seol, K. Jarvis, Pore-Scale Visualization of Methane Hydrate-Bearing Sediments With Micro-CT, Geophysical Research Letters 45 (2018) 5417-5426.

[33] L. Yang, A. Falenty, M. Chaouachi, D. Haberthür, W.F. Kuhs, Synchrotron X-ray computed microtomography study on gas hydrate decomposition in a sedimentary matrix, Geochemistry, Geophysics, Geosystems 17 (2016) 3717-3732.

[34] S. Almenningen, J. Flatlandsmo, A.R. Kovscek, G. Ersland, M.A. Ferno, Determination of pore-scale hydrate phase equilibria in sediments using lab-on-a-chip technology, Lab Chip 17 (2017) 4070-4076.

[35] L. Zhang, C. Zhang, K. Zhang, L. Zhang, J. Yao, H. Sun, Y. Yang, Pore-Scale Investigation of Methane Hydrate Dissociation Using the Lattice Boltzmann Method, Water Resources Research 55 (2019) 8422-8444.

[36] X. Wang, B. Dong, C. Chen, W. Li, Y. Song, Pore-scale investigation on the influences of mass-transfer-limitation on methane hydrate dissociation using depressurization, International Journal of Heat and Mass Transfer 144 (2019) 118656.

[37] J. Latt, O. Malaspinas, D. Kontaxakis, A. Parmigiani, D. Lagrava, F. Brogi, M.B. Belgacem, Y. Thorimbert, S. Leclaire, S. Li, F. Marson, J. Lemus, C. Kotsalos, R.

Conradin, C. Coreixas, R. Petkantchin, F. Raynaud, J. Beny, B. Chopard, Palabos: Parallel Lattice Boltzmann Solver, Computers & Mathematics with Applications 81 (2021) 334-350.

[38] X. Wei, W. Li, Q. Liu, W. Sun, S. Liu, S. Li, H. Wei, L. Ma, Pore-scale investigation on multiphase reactive transport for the conversion of levulinic acid to γ-valerolactone with Ru/C catalyst, Chemical Engineering Journal 427 (2022) 130917.

[39] L. Chen, R. Zhang, Q. Kang, W.Q. Tao, Pore-scale study of pore-ionomer interfacial reactive transport processes in proton exchange membrane fuel cell catalyst layer, Chemical Engineering Journal 391 (2020) 123590.

[40] H. Kim, P.R. Bishnoi, R.A. Heidemann, S.S. Rizvi, Kinetics of methane hydrate decomposition, Chemical Engineering Science 42 (1987) 1645-1653.

[41] V.A. Kamath, Study of heat transfer characteristics during dissociation of gas hydrates in porous media, Pittsburgh Univ., PA (USA), 1984.

[42] G.J. Moridis, TOUGH+ HYDRATE v1. 2 User's manual: a code for the simulation of system behavior in hydrate-bearing geologic media, (2012).

[43] K. Sell, E.H. Saenger, A. Falenty, M. Chaouachi, D. Haberthür, F. Enzmann, W.F. Kuhs, M. Kersten, On the path to the digital rock physics of gas hydrate-bearing sediments – processing of in situ synchrotron-tomography data, Solid Earth 7 (2016) 1243-1258.

[44] A. Fukumoto, K. Kamada, T. Sato, H. Oyama, H. Torii, F. Kiyono, J. Nagao, N. Temma, H. Narita, Numerical simulation of pore-scale formation of methane hydrate in the sand sediment using the phase-field model, Journal of Natural Gas Science and

Engineering 50 (2018) 269-281.

[45] J. Hou, Y. Ji, K. Zhou, Y. Liu, B. Wei, Effect of hydrate on permeability in porous media: Pore-scale micro-simulation, International Journal of Heat and Mass Transfer 126 (2018) 416-424.

[46] D.H. Kang, T.S. Yun, K.Y. Kim, J. Jang, Effect of hydrate nucleation mechanisms and capillarity on permeability reduction in granular media, Geophysical Research Letters 43 (2016) 9018-9025.

[47] X. Chen, R. Verma, D.N. Espinoza, M. Prodanović, Pore-Scale Determination of Gas Relative Permeability in Hydrate-Bearing Sediments Using X-Ray Computed Micro-Tomography and Lattice Boltzmann Method, Water Resources Research 54 (2018) 600-608.

[48] T. Krüger, H. Kusumaatmaja, A. Kuzmin, O. Shardt, G. Silva, E.M. Viggen, The lattice Boltzmann method, Springer International Publishing 10 (2017) 4-15.

[49] J. Yang, X. Dai, Q. Xu, Z. Liu, L. Shi, W. Long, Lattice Boltzmann modeling of interfacial mass transfer in a multiphase system, Physical Review E 104 (2021) 015307.

[50] X. Shan, H. Chen, Lattice Boltzmann model for simulating flows with multiple phases and components, Phys Rev E Stat Phys Plasmas Fluids Relat Interdiscip Topics 47 (1993) 1815-1819.

[51] M.L. Porter, E.T. Coon, Q. Kang, J.D. Moulton, J.W. Carey, Multicomponent interparticle-potential lattice Boltzmann model for fluids with large viscosity ratios, Phys Rev E Stat Nonlin Soft Matter Phys 86 (2012) 036701.

[52] S. Mukherjee, P. Berghout, H.E.A. Van den Akker, A lattice boltzmann approach

to surfactant-laden emulsions, AIChE Journal 65 (2019) 811-828.

[53] Q. Li, Z. Chai, B. Shi, H. Liang, Deformation and breakup of a liquid droplet past a solid circular cylinder: a lattice Boltzmann study, Phys Rev E Stat Nonlin Soft Matter Phys 90 (2014) 043015.

[54] S.P. Sullivan, F.M. Sani, M.L. Johns, L.F. Gladden, Simulation of packed bed reactors using lattice Boltzmann methods, Chemical Engineering Science 60 (2005) 3405-3418.

[55] Y. Haroun, D. Legendre, L. Raynal, Volume of fluid method for interfacial reactive mass transfer: Application to stable liquid film, Chemical Engineering Science 65 (2010) 2896-2909.

[56] Y.L. He, Q. Liu, Q. Li, W.Q. Tao, Lattice Boltzmann methods for single-phase and solid-liquid phase-change heat transfer in porous media: A review, International Journal of Heat and Mass Transfer 129 (2019) 160-197.

[57] H. Karani, C. Huber, Lattice Boltzmann formulation for conjugate heat transfer in heterogeneous media, Phys Rev E Stat Nonlin Soft Matter Phys 91 (2015) 023304.

[58] Q. Kang, P.C. Lichtner, D. Zhang, Lattice Boltzmann pore-scale model for multicomponent reactive transport in porous media, Journal of Geophysical Research: Solid Earth 111 (2006) B05203.

[59] C. Soulaine, S. Roman, A. Kovscek, H.A. Tchelepi, Mineral dissolution and wormholing from a pore-scale perspective, Journal of Fluid Mechanics 827 (2017) 457-483.

[60] Y. Masuda, Numerical calculation of gas production performance from reservoirs

containing natural gas hydrates, Annual Technical Conference, Soc. of Petrol. Eng., San Antonio, Tex., Oct. 1997, 1997.